

LAPPEENRANTA UNIVERSITY OF TECHNOLOGY
LUT School of Engineering Science
Degree Programme in Technical Physics

Aleksandr Dubov

Finite size effects in superconducting nanocomposites

Examiners: Prof. Erkki Lähderanta
D. Sc. Ivan Zakharchuk

ABSTRACT

Lappeenranta University of Technology
LUT School of Engineering Science, Department of Physics
Degree Programme in Technical Physics

ALEKSANDR DUBOV

FINITE SIZE EFFECTS IN SUPERCONDUCTING NANOCOMPOSITES

Master's thesis
2015

54 pages, 17 figures, 2 tables

Examiners: Prof. Erkki Lähderanta
D. Sc. Ivan Zakharchuk

Keywords: Superconductivity, Nanoscale, Nanoparticles, Nanocomposites, Phase fluctuations, Shell effects, Disorder effects

The present Master's thesis presents theoretical description of the extraordinary behavior of the confined Indium nanoparticles. Superconducting properties of nanoparticles and nanocomposites are extensively reviewed. Special attention has been paid to phase fluctuation, shell and disordered effects. The experimental data has been obtained and provided by Dmitry Shamshur from Ioffe Physical Technical Institute. The investigated material represents a highly ordered system of silicate spheres filled with indium metal, where the In nanoparticles are interconnected between each other. Bulk indium is a superconductor with critical superconducting temperature $T_{c0} = 3.41$ K. But indium nanoparticles exhibit different behavior, the critical temperature rise by approximately 20% up to 4.15 K. As well as transition of the indium particles to type-II superconductivity with high critical magnetic fields. Such diversity is explained by finite size effects which originate from nanosize of the samples.

1	Introduction	3
1.1	Superconducting nanoparticles	3
1.2	Superconducting mono-layer films	5
1.3	Superconducting nanocomposites	5
2	Shell and inhomogeneous pairing effects	11
3	Enhancement of superconductivity by engineered nanogranularity	21
4	Phase fluctuations and shell effects in Indium nanocomposites	29
4.1	Sample characterization	30
4.2	Superconducting transitions	35
4.3	Thermomagnetic instabilities in magnetization	40
5	Conclusion	45
	Bibliography	46

The emergence of size-dependent superconducting critical temperature T_c has been found as one of the intriguing issue in low temperature superconducting nanoparticles and nanocomposites, because of opposite behavior of various materials. The theoretical mechanisms of this behavior are also under debates. The investigation of size effects on low temperature superconductivity can be divided in three categories: superconducting nanoparticles, superconducting thin films, and superconducting nanocomposites. All these directions of investigations are highlighted below in the literature overview.

1.1 Superconducting nanoparticles

Quantum size effects (QSE) play crucial role in zero dimensional superconductors (Delft (2001); Anderson (1959)). The superconductivity can be suppressed by QSE but also result in novel phenomena like shell effects. The shell effects are predicted to greatly enhance the superconducting energy gap (Kresin and Ovchinnikov (2006); M.Garcia-Garcia et al. (2008); Olofsson et al. (2008)). The experimental evidence for QSE has been observed in Ref. (Bose et al. (2010)) through measurements on single, isolated Pb and Sn nanoparticles. In both systems superconductivity has been suppressed at small sizes, where quantum fluctuations of the order parameter are strong. However, at smaller scale, before the destruction of superconductivity, in Sn nanoparticles giant oscillations in the superconducting energy gap have been observed. The superconductivity has improved by 60%. On the contrary, the lead nanoparticles have not shown any gap oscillations which could be understood as a decrease of shell effects for shorter coherence lengths.

Another important issue of zero dimensional superconductivity are thermal fluctuations. The authors of Ref. (Brihuega et al. (2011)) observed superconductivity beyond T_c in single, isolated Pb nanoparticles with sizes $h \leq 13$ nm. They showed through quantitative calculations that these deviations from mean-field predictions are caused by thermal fluctuations. Moreover, at temperatures much lower than critical ($T \ll T_c$) thermal fluctuations are small and at sizes of particles below 20

nm, energy gap Δ decreases with reduction of particle size. The high energy resolution scanning tunneling spectroscopy study on 8-9 monolayer thick Pb islands by Liu *et al* (Liu et al. (2013)) has revealed a critical region in superconductivity originating from fluctuations. The superconducting transition temperatures gradually suppress when the size of the Pb islands decrease. The reduction in size leads to changes of the density of states (DOS) at the Fermi level E_F due to the discretization of electronic levels resulting in lower critical temperature. This behavior is completely different from the sudden drop of T_c observed in the system of ensemble of lead particles (Liu et al. (2013)). The limiting size of a nine-monolayer-thick Pb island with superconductivity above 3.2 K has been determined to be $\sim 30 \text{ nm}^2$, in good agreement with the Anderson criterion (Liu et al. (2011)). It turns out that the zero-temperature energy gap Δ_0 reduces considerably faster than the critical temperature when the lead island size approaches this limit. However, the decrease of $2\Delta(0)/k_B T_c$ from 4.5 to 3.3 indicate that superconducting coupling in Pb islands changes from strong to weak electron-phonon interactions.

From the theoretical point of view, described above systems of superconducting nanoparticles can be modeled as isolated superconducting nanocubes. Mayoh and Garcia-Garcia (Mayoh and Garcia-Garcia (2014a)) analytically have studied superconductivity in isolated superconducting nanocubes and nanosquares of size L in the limit of negligible disorder $\delta/\Delta_0 \ll 1$ and $k_F L \gg 1$, where k_F is the Fermi wave vector, δ is the mean level spacing, and Δ_0 is the bulk gap. The size scale of $L \sim 10 \text{ nm}$ is still appropriate for mean-field theory and semiclassical approaches. It has been found that the size effects are important and result in deviations of energy gap from the bulk value even at relatively large size of superconducting grains $L \sim 50 \text{ nm}$.

More evidence, that particle size dependence of superconductivity rise from the changes in the electronic density of states, has been presented in Ref. (Bose et al. (2005b)). The investigation of nanostructured Nb films has shown that the superconducting energy gap decreases with a reduction in the average particle size. Simultaneously, the superconducting critical temperature also reduces with the size in such a way that the energy gap and critical temperature have a direct correlation between each other. The Anderson limit of the superconducting size in nanostructured films of Nb is 8 nm. Below this particle size no superconductivity has emerged.

Additionally, Bose *et al* (Bose et al. (2006)) have shown that the upper critical field in nanometer-sized Nb particles is governed by the changes in the effective Ginzburg-Landau coherence length. As well as the decrease of the density of states at the Fermi level, the decrease in the grain size leading to the increase of disorder can drastically influence the effective coherence length. As a result, the upper critical field in nanostructured Nb show nonmonotonic grain size dependences at relatively large grain size (20-60 nm). On the other hand, the negligible changes of the T_c with grain size reduction point to the growth of disorder, which diminishes the mean free path and, consequently, the coherence length. Further size reduction (<20 nm) results in a quantization of the electronic energy levels and consequent decrease in the density of states at the Fermi level, which

leads to reduction of the H_{c2} and vanishing of superconductivity.

1.2 Superconducting mono-layer films

Modern nanotechnology has given rise to investigations of ultrathin superconducting films of high crystallinity. At the same time, measurements of such two-dimensional (2D) structures require ultra-high vacuum and low temperatures. Despite the obstacles, the existence of macroscopic superconductivity has been observed by direct electron transport measurements on a silicon surface reconstruction with In adatoms [Si(111)-($\sqrt{7} \times \sqrt{3}$)-In] (Uchihashi et al. (2011)). The superconducting critical temperature for such system is 2.8 K being 18% less than the bulk Indium transition temperature.

The voltage-current characteristics show sharp and hysteretic transition between superconducting and normal states with well-defined critical and retrapping currents (Uchihashi et al. (2011)). The two-dimensional critical current density $J_{2D,c}$ is estimated to be as high as 1.8 A/m at 1.8 K. The atomic steps present in the structure act as strongly coupled Josephson junctions. Another study on Si(111)-($\sqrt{7} \times \sqrt{3}$)-In surface by Yamada *et al* (Yamada et al. (2013)) has reported similar critical temperature of 2.8 K for rectangular phase, and 2.4 K for the hexagonal phase of In adatoms. The upper critical field of this structure has been found to be 0.1-1 T from magnetotransport measurements with magnetic field perpendicular to the surface.

The Ginzburg-Landau coherence length calculated from the upper critical field is of the order of tens of nanometers. The Pippard's coherence length computed from the band structure parameters revealed a value of the micrometer order. However, for pure materials Ginzburg-Landau coherence length should be approximately equal to Pippard's one. This discrepancy suggests that the coherence length is limited by the mean free path due to the defects on the silicon surface as well as the fluctuations of the superconducting energy gap influence.

1.3 Superconducting nanocomposites

There are at least two counteracting effects that change T_c in nanostructured superconductors. One of them arises from the increase in surface to volume ratio due to the decrease of the particle size. The increased number of surface phonons, which are softer than bulk phonons, results in an enhanced electron-phonon coupling and, consequently, higher critical temperatures. But this enhancement can be lowered or even be negative when the discretization of the electronic energy bands occurs with particle size reduction. The discretization decreases the effective density of states at the Fermi level and, therefore, the overall superconductivity.

To distinguish between these two effects, separate investigation of the energy gap and critical temperature is needed. A good experiment has been conducted by the authors of Ref. (Bose et al.

(2009)). They explored the influence of the two mechanisms on T_c over a large particle size range in nanostructured Pb by measuring the temperature dependence of the superconducting energy gap in planar tunnel junctions of Al/Al₂O₃/nano-Pb. It has been shown that the superconducting transition temperature reduces gradually with the Pb particle size and, in contrast, the upper critical field is greatly enhanced in the same size range. The electron-phonon coupling increases monotonically with decreasing particle size at nanoparticle sizes less than 22 nm. Such increase in Cooper pair coupling almost exactly compensates for the quantum size effect. But at particle sizes below 7 nm, quantum size effect wins and, in agreement with the Anderson limit, superconductivity is completely suppressed.

The enhancement of the critical temperature of nanostructured superconductors in comparison to their bulk T_c can be also attributed to the emergence of surface superconductivity. The experimental observation of the surface superconductivity is hampered by the bulk superconductivity. Thus, surface superconductivity can be seen only when the bulk superconductivity is greatly suppressed or absent. This is the case when the surface superconductivity T_c is higher than that of the bulk superconductivity. Surface superconductivity need only a weak attraction among particles, which come from the partially filled surface levels, to form correlated pairs. Additionally, the transition of non-localized surface electrons to superconducting state, and their interaction with surface phonons can produce additional attraction among electrons located close to the surface area (Panova et al. (2008)).

Heat capacity measurements of lead embedded in glass nanopores done in Ref. (Panova et al. (2008)) show two superconducting transitions, one positioned above and another below the critical temperature of the bulk lead material. The higher temperature is ascribed to the surface superconductivity and the lower corresponds to the volume superconductivity. The upper critical fields H_{c3} for the surface superconductivity and H_{c2} for the volume superconductivity exceed the critical field of the bulk Pb by 140 and 70 times, respectively. Hence, the corresponding ratio is $H_{c3}/H_{c2} \approx 2$, which is larger than the theoretical 1.7.

Studies of ac and dc magnetization and heat capacity in a superconducting lead-porous glass nanocomposite were carried out in Ref. (Ciou et al. (2012)). Double anomalies were found on their temperature dependences at different magnetic field. The positions of anomalies of heat capacity and ac and dc magnetization correlated with each other. The additional, low-temperature anomalies shifted remarkably with increasing magnetic field. The field cooled and field-cooled-warming curves observed upon cooling and warming, respectively, showed thermal hysteresis at the second step. The peak effect on magnetization loops was seen above 6 K. The low-temperature anomalies in the ac and dc magnetization were treated as a manifestation of transformation in the vortex system which is triggered by superconductivity in confined lead islands.

An ac magnetization technique was used to study superconductivity in tin loaded nanoporous silica matrices, opal matrix and two porous glasses (Ciou et al. (2013)). The behavior of type-II

superconductors with a sharp transition at zero bias field was observed. Regular increase in the superconducting temperature up to 4.2 K and in a critical field up to $H_{c2}(0) \approx 54$ kOe with decreasing pore size was found. A crossover from the upturn to the common downturn curvature in the $H_{c2}(T)$ line was seen for all nanocomposites; the upturn curvature was more pronounced for the matrix with the finest pores.

The synthesis of biphasic Pb (46 at.%)–Sn (54 at.%) nanoparticles dispersed in an aluminum matrix has been reported and the nature of the superconducting transition in these particles has been explored (Bose et al. (2008)). The nanoscaled Pb–Sn alloy particles were dispersed in Al by rapid solidification and the two-phase nature of these particles was characterized by transmission electron imaging, diffraction and composition mapping. A weak superconducting transition occurs at 3.1 K in these alloys, which is much lower than the T_c expected for a Pb (46 at.%)–Sn (54 at.%) alloy or that due to the proximity effect between Pb and Sn. It has been shown that it is the superconducting Al matrix with $T_c = 1.2$ K that plays a major role in determining the effective transition temperature of the system.

Nanoembedded biphasic alloy particles of In–Sn near eutectic alloy compositions embedded in an aluminium matrix by rapid solidification processing has been synthesized in Ref. (Bose et al. (2005a)). Detailed transmission electron microscopy indicates that the two phases present at room temperature in as-synthesized samples are β and γ phases with tetragonal and hexagonal crystal structures, respectively. These co-exist with a small amount of single phase In or Sn particles with sizes less than 10 nm. Low temperature magnetization measurements indicate a superconducting transition temperature of 5 K, suggesting complete decomposition of the β -phase at small sizes and at low temperature. The small particles show type-II behavior with a critical field $H_{c1} \approx 44$ G and two values for H_{c2} of 250 and 1000 G, respectively. These values are considerably lower than those observed in bulk In–Sn alloys.

Tien *et al* (Tien et al. (2000)) studied indium and gallium in porous glass by resistance and magnetization measurements. For indium in porous glass, a very sharp superconducting transition is observed at $T_1 = 4.0 \pm 0.05$ K. When a 1.5 T magnetic field is applied, there is a second transition at $T_2 \sim 3.5$ K. At 3.5 K, the field dependence of resistance $R(H)$ indicates two transitions at $H_c^u \sim 1.4$ and $H_c^l \sim 0.4$ T separated by a plateau. For indium in porous glass, the origins of two-step transitions in $R(T)$ and $R(H)$ might be the same. At H_c^u (or T_1) the individual grains of indium in porous glass become superconductors and at H_c^l (or T_2) all grains are coupled. For gallium in porous glass, two superconducting transitions of $R(T)$ at $T_1 = 7.0$ and $T_2 = 6.3$ K are observed. Between 6.35 and 6.30 K, $R(T)$ increases sharply with decreasing temperature. The quasiparticle tunneling or the conductor-superconductor-conductor coupling might cause the sharp rise in resistance between 6.35 and 6.30 K. At 6 K, there are two transitions at $H_c^u = 2.1$ T and $H_c^l = 1.1$ T in the $R(H)$ for gallium in porous glass. The two different transitions of $R(H)$ might be caused by a filamentary internal structure of gallium crystallites. There is no diamagnetism at T_1 . The magnetic

transition temperature has been found to be $T_M < T_2$ for T_M measured at 3, 4, 5, 6, and 7 T.

The superconducting transition of indium in 56 Å pore Vycor glass has been studied in Ref. (Graf et al. (1992)) through resistance and magnetic susceptibility measurements. The confined indium behaves like a dirty type-II superconductor, and the superconducting transition consists of two transitions, which become well separated in applied magnetic fields. While the lower critical field H_{c1} follows de Gennes's prediction of $H_{c2}(T)$, the higher critical field H_c^u has an unusual dependence of $(1 - T/T_c)^{1/2}$. The possible origin of this transition is discussed in terms of the microstructure of the composite.

Superconductivity and crystalline structure were studied for two nanocomposites consisting of gallium loaded porous glasses with different pore sizes (Charnaya et al. (2009)). The superconducting transition temperatures were found to differ from those in known bulk gallium modifications. The transition temperatures 7.1 and 6.7 K were ascribed to two new confined gallium structures, i - and κ -Ga, observed by synchrotron radiation x-ray powder diffraction. The evolution of superconductivity on decreasing the pore filling with gallium was also studied. The complex crystalline structure of gallium under nanoconfinement was revealed by synchrotron radiation x-ray powder diffraction (Lee et al. (2010)). Nanoconfinement was shown to stabilize δ -Ga which is metastable in bulk. Two new gallium phases named i - and κ -Ga were found upon cooling below room temperature. These crystalline modifications were stable and coexisted with known gallium phases. Correlations between confined gallium particle shapes and emergence of particular crystalline phases were observed. Melting and freezing temperatures for different gallium phases were obtained. Remarkable supercooling of liquid gallium was seen in 3.5 nm pores.

The material dependent behavior can be reasonably explained by shell effects in nanoparticles (Kresin and Ovchinnikov (2006); M.Garcia-Garcia et al. (2008); Olofsson et al. (2008); Bose et al. (2010); Mayoh and Garcia-Garcia (2013)) and nanocomposites (Ghosh and Mandal (2013); Mayoh and Garcia-Garcia (2014b)). It is shown in this theory (Mayoh and Garcia-Garcia (2014b)) that the value of the Bardeen-Cooper-Schrieffer (BCS) coupling constant λ plays an important role in T_c . The larger the λ , the less important size effects are. This follows from the fact that the coherence length ξ decreases as λ increases thus making the material more bulk-like. This prevents the employment of BCS theory based approach in the study of cuprates and other strongly coupled superconductors. Indeed, the superconductors with lower critical temperature, such as Ga, In, Sn, exhibit the T_c increasing with decreasing of size while strong coupling superconductors, such as Nb and Pb, do not show it. Besides the predictions about the importance of the coupling constant there are other significant results of the shell effect theory in nanocomposites: nonmonotonous T_c^{Array} dependences from the normal state array resistance values and strong array geometry dependence. The highest T_c^{Array} has been found for intermediate resistances and for face-centered cubic (FCC) array. In Sections 2 and 3 the shell effects in superconducting nanoparticles and nanocomposites are discussed.

Another important aspect of physics of nanocomposites is phase fluctuation which appears in disordered superconductors. It has been a long-standing paradigm in superconductivity that the properties of the superconducting state are not affected by disorder (Anderson (1959)). Consequently, it has become a justified practice to expect a fixed critical temperature T_c for superconducting films, directly related to a standard BCS gap and quasiparticle density of states, irrespective of large differences in normal state resistivity. On the other hand, theoretical evidence has been developed that reveals severe deviations from BCS theory for materials with a resistivity in the range $100 \mu\Omega\cdot\text{cm}$ and higher. In materials with such a large resistivity, the elastic scattering length l is of the order of the interatomic distance. Therefore, it can be expected that localization effects become important. From numerical simulations it has become clear that, even for homogeneous disorder, eventually an inhomogeneous superconducting state will arise when the disorder is increased (Ghosal et al. (1998)). A short elastic scattering length enhances both the Coulomb interaction between electrons (Finkelstein (1987)), and the interference of electrons scattering from impurities. These mesoscopic fluctuations were shown to grow when approaching the superconductor-to-insulator transition (SIT) (Skvortsov and Feigel'man (2005)), and unavoidably affect the properties of the superconducting state (Feigel'man and Skvortsov (2012)). The effects of strong disorder ($2.4 < k_F l < 8.6$) on superconductivity in thin films of niobium titanium nitride and titanium nitride was investigated in Ref. (Driessen et al. (2012)) by measuring the microwave electrodynamics in coplanar waveguide resonators. The gradual evolution of the electromagnetic response with disorder, deviating from BCS theory, for both materials was observed. Strong suppression of T_c was observed for thin films with normal state resistivities exceeding $\mu\Omega\cdot\text{cm}$. This result can be understood as due to changes in the quasiparticle density of states, induced by the short elastic scattering length (Feigel'man and Skvortsov (2012)). The observations are consistent with a model using an effective pair breaker, dependent on the level of disorder.

Many different material systems undergo a superconductor-insulator transition in the limit of two dimensions and zero temperature ($T = 0$) by the variation of a tuning parameter such as disorder, an applied magnetic field, or charge density (Goldman and Markovic (1998); Gantmakher and Dolgoplov (2010)). Theoretical approaches to explain SITs have to deal with the question of how superconductivity disappears with increasing disorder. Here the interplay of the attractive and repulsive electron-electron interactions plays a crucial role. In the theory of boson localization (Fisher (1990)) (also dirty-boson or Bose-glass model), a continuous SIT is predicted at $T = 0$ as a result of the competition between quantum phase fluctuations and long-range Coulomb repulsion. The evolution of two-dimensional electronic transport with increasing disorder in epitaxial FeSe thin films was studied in Ref. (Schneider et al. (2012)), where the disorder had been generated by reduction of the film thickness. As a result increasing of the resistivity and strong reducing of T_c was observed. The extreme sensitivity of the films to disorder results in a superconductor-insulator transition. The finite-size scaling analysis in the critical regime based on the Bose-glass model strongly supports

the idea of a continuous quantum phase transition. The theory of phase fluctuations in nanogranular superconductors is discussed in Sections 3 and 4.

Another peculiarity of the superconducting nanocomposites is a transformation of the behavior from type-I to type-II and vortices are formed in the external magnetic field. The superconductivity of gallium in porous glasses with various pore sizes and in opals is studied using a superconducting quantum interference device magnetometer (Charnaya et al. (1998)). The single and double superconducting phase transitions are observed for different samples. Magnetization hysteresis loops are also measured and found to be dependent on pore sizes and geometry. The changes in magnetization below about 6.4 K are treated within the framework of models for granular superconductors, while the alterations in magnetization near 7.1 K are treated as a result of the superconducting phase transition in a coexistent structural modification of confined gallium. X-ray diffraction measurements are performed to confirm the presence of such an additional gallium modification. The results suggested that studies of magnetization at low temperatures can be used to get information about the geometry of the pore network and distribution of Josephson links in porous composite materials.

Ac magnetization measurements were carried out for a gallium nanocomposite consisted of a metal loaded porous glass with 3.5 nm pore size to study dynamics in the vortex system and $H - T$ diagrams (Lee et al. (2013)). Variations of ac magnetization with temperature and bias magnetic field were obtained at different frequencies and amplitudes of ac field. Double peaks in the imaginary part of ac susceptibility associated with doubly structured real parts with distinct dependences on the amplitude of ac field were observed. Activation barriers were evaluated from variations with frequency of the upper-temperature peak in χ'' at different bias fields. The field dependence of the activation barrier followed the power law with exponents equal to 0.12 and 1.0 below and above 20 kOe, respectively. A pronounced positive curvature was observed at low magnetic fields for the $H_{c2}(T)$ line with the crossover to a common negative curvature near 20 kOe, also. Both the change of the exponent in the power law for activation barriers and the crossover to the negative curvature in the upper critical field line were suggested to occur due to transition in the vortex system from the geometry restricted to space between gallium particles into more homogeneous distribution with increasing field.

Chapter 4 presents the description of experimental results and their theoretical explanation. Peculiar features of magnetization curves are discussed from the point of view of thermomagnetic instabilities and fluxoid transitions. The results are compared with different theoretical models as well.

Shell and inhomogeneous pairing effects

Downscaling a superconductor and enhancing superconductivity has been a major challenge in the field of nanoscale superconductivity. The advent of new tools of nanotechnology for both synthesis and measurement of single, isolated mesoscopic superconducting structures has opened up the possibility to explore novel and fascinating phenomena at reduced dimensions (Ralph et al. (1995); Bezryadin et al. (2000); Shanenko et al. (2006b)). One of them, the parity effects in the superconducting energy gap, was demonstrated almost two decades ago in the only experiments which have been able to access the superconducting properties of an individual nanoparticle (Ralph et al. (1995)) till date. Another exciting prediction is the occurrence of shell effects in clean, superconducting nanoparticles (M.Garcia-Garcia et al. (2008)).

The origin of shell effects is primarily due to the discretization of the energy levels in small particles which leads to substantial deviations of the superconducting energy gap from the bulk limit. For small particles, the number of discrete energy levels within a small energy window (pairing region) around the Fermi energy (E_F) fluctuates with very small changes in the system size. Consequently this leads to fluctuations in the spectral density around E_F . Since in weakly coupled superconductors electronic pairing mainly occurs in a window of size E_D (Debye energy) around E_F , an increase (decrease) of the spectral density around E_F will make pairing more (less) favorable, thereby increasing (decreasing) the energy gap. As a consequence the gap becomes dependent on the size and the shape of the particle (see schematic drawing in Fig. 2.1). The strength of fluctuations also increases with the symmetry of the particle, since symmetry introduces degeneracies in the energy spectrum. It is easy to see that these degenerate levels will enhance the fluctuations in the spectral density and also in the gap as the number of levels within $\pm E_D$ of E_F , and consequently the number of electrons taking part in pairing, fluctuates dramatically. These degenerate levels are referred to as "shells" in analogy with the electronic and nucleonic levels forming shells in atomic, cluster and nuclear physics (see Ref. (Kresin and Ovchinnikov (2006)) and references therein). For cubic or spherical particles this might lead to a large modification of Δ . Theoretically, these shell effects are

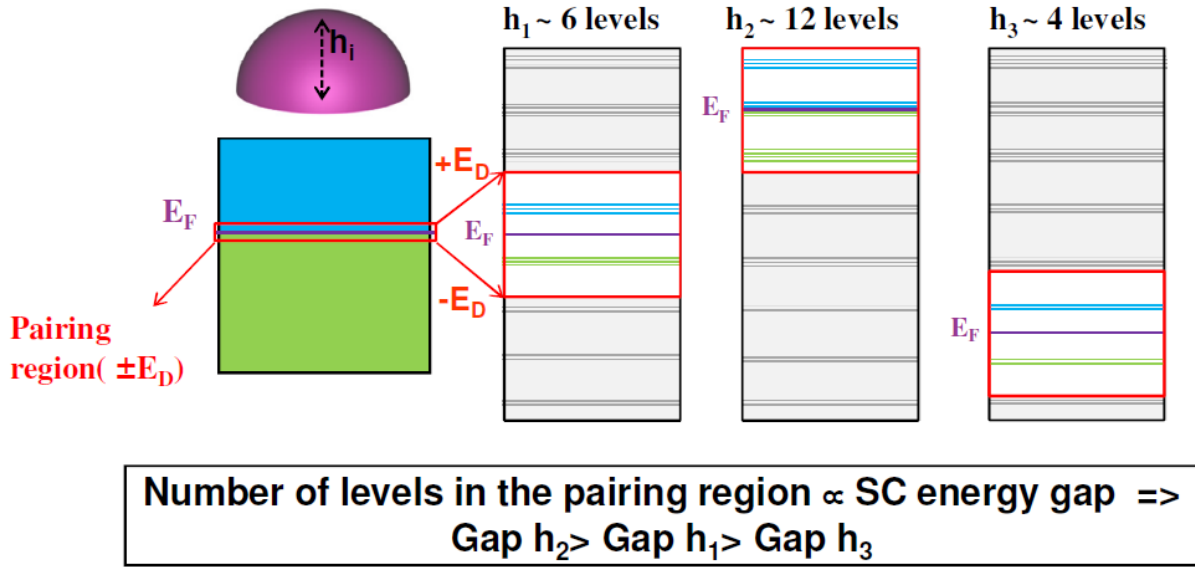


Figure 2.1: Schematic of shell effects. Schematic explaining the physical origin of shell effects in small particles which leads to an oscillation in the gap value with particle size. The hemisphere in the upper left corner represents a nanoparticle with height h_i deposited on a substrate. Below the nanoparticle its energy band diagram is shown. As the particle is very small, quantum effects start to exhibit themselves by the discretization of the energy levels. Each degenerate level in a small particle is referred to as the "shell". Only electrons which are near the Fermi level E_F take part in pairing and superconductivity. Therefore, only the electronic levels around the Fermi level are relevant for superconductivity. The expansion of this pairing region is shown for three particles with heights h_1 , h_2 and h_3 which are very close to each other. The number of levels in this pairing window fluctuates depending on the position of the Fermi level in the three particles which leads to the fluctuation in the gap (shell effects). From Ref. (Bose et al. (2010)).

described quantitatively by introducing finite size corrections to the BCS model (M.Garcia-Garcia et al. (2008); Olofsson et al. (2008)). In Ref. (Bose et al. (2010)) authors investigated individual superconducting nanoparticles of Pb and Sn with scanning tunneling spectroscopy. The existence of shell effects has been observed for the first time and the influence of the superconducting coherence length on them has been demonstrated.

Fig. 2.2a shows the schematic of the experimental measurement where an STM tip is used to measure the tunneling density of states (DOS) of superconducting nanoparticles of both Pb and Sn. A typical representative STM topographic image for Sn nanoparticles (for Pb nanoparticle topographic image, see Ref. (Brihuega et al. (2011))) with varying size on a BN/Rh(111) substrate is shown in Fig. 2.2b. The height of the nanoparticle has been taken as reference since it can be measured with a high degree of accuracy with the STM. The quasiparticle excitation spectra (conductance plots of dI/dV vs V normalized at +5mV) for a selection of Pb and Sn nanoparticles at a temperature of 1.2-1.4 K are presented in Figs. 2.2c-e. Each spectrum is fitted with the tunneling

equation, (Tinkham (1996))

$$G(V) = \left. \frac{dI}{dV} \right|_V = G_{nn} \frac{d}{dV} \left\{ \int_{-\infty}^{\infty} N_s(E) f(E) - f(E - eV) dE \right\} \quad (2.1)$$

Where $N_s(E)$ is the DOS of the superconductor, $f(E)$ is the Fermi-Dirac distribution function and G_{nn} is the conductance of the tunnel junction for $V \gg \Delta/e$. The density of states $N_s(E)$ is given by:

$$N_s(E, \Gamma, T) = \text{Re} \left[\frac{|E| + i\Gamma(T)}{\sqrt{(|E| + i\Gamma(T))^2 - \Delta(T)^2}} \right] \quad (2.2)$$

Where, $\Delta(T)$ is the superconducting energy gap and $\Gamma(T)$ is a phenomenological broadening parameter which incorporates all broadening arising from any non-thermal sources (conventionally it is associated with the finite lifetime (τ) of the quasiparticles, $\Gamma \sim \hbar/\tau$) (Dynes et al. (1978)). There is an excellent agreement between the experimental data and the theoretical fits, giving unique values of Δ and Γ (plotted as a function of particle size in Fig. 2.2f and 2.2g, respectively). One can see that there is a gradual decrease in the zero bias conductance dip with particle size for Pb nanoparticles (Fig. 2.2c), while for Sn nanoparticles (Figs. 2.2d and 2.2e) there is a non monotonic behavior which strongly depends on the particle size regime. The large Sn particles (>20 nm) differing in a size of 1 nm have similar DOS signifying similar gaps, there is a large difference in the DOS and hence Δ , for the smaller Sn particles (< 15 nm) even if they differ by less than 1 nm in size. The difference in the two systems is brought out more clearly in Fig. 2.2f where the normalized gap is plotted (normalized with respect to their bulk values). For Pb, Δ decreases monotonically with decrease in particle size while there is a huge variation in the gap values for Sn below a particle size of 20 nm. For these small sizes, gap values differ even more than 100% for similar sized Sn particles and enhancements as large as 60% with respect to the bulk Sn gap has been found. In both systems however, superconductivity is destroyed below a critical particle size which is consistent with the Anderson criterion (Anderson (1959)), according to which superconductivity should be completely destroyed for particle sizes where the mean level spacing becomes equal to the bulk superconducting energy gap (Delft et al. (1996)). It is also worth noting that the average gap for the large Sn nanoparticles (20-30 nm) shows an increase of 20% from the bulk value.

From the two parameters characterizing the superconducting state of the nanoparticles, Δ and Γ , only Γ evolves in a similar way as a function of particle size both for Pb and Sn (Fig. 2.2g). In both systems, an increase in Γ with reduction in particle size has been observed. Interestingly, it seems that superconductivity is limited to sizes where $\Gamma < \Delta_{\text{bulk}}$. At smaller sizes superconductivity is completely suppressed in both systems. This indicates that Γ may have a particular significance. To understand the behaviour of Γ with particle size Bose *et al* linked it to quantum fluctuations in small

particles (Bose et al. (2010)). It is known from both theoretical calculations and experiments that there should be an increase in the quantum fluctuations in confined geometries (Dynes et al. (1984); Skocpol and Tinkham (1975); Bennemann and Ketterson (2008)) as observed by Bezryadin *et al* in their experiments on nanowires (Bezryadin et al. (2000)). Similarly, since in a zero dimensional superconductor the number of electrons taking part in superconductivity decreases, an increase in the uncertainty in the phase of the superconducting order parameter is expected (Tinkham (1996); Dynes et al. (1978)) (within a single particle, there will be a decrease in the long range phase coherence). The increased fluctuations in the superconducting order parameter are expected to increase Γ (as fluctuations act as a pair breaking effect). Therefore, Γ can be associated with the energy scale related with quantum fluctuations. The results in Ref. (Bose et al. (2010)) indicate that in zero dimensional systems the presence of quantum fluctuations of the phase (where $\Gamma > \Delta_{\text{bulk}}$) set the limit to superconductivity and this corresponds to the size consistent with the Anderson criterion (Bennemann and Ketterson (2008)).

In order to interpret the variation of Δ with particle size in Sn nanoparticles, and the observed striking difference with Pb, a theoretical study of finite size corrections in the BCS formalism has been carried out by Bose *et al* (Bose et al. (2010)) in line with references (M.Garcia-Garcia et al. (2008); Olofsson et al. (2008)). They has been focused on the finite size corrections to the BCS gap equation since the corrections to the BCS mean field approximation leads to a monotonic decrease in the gap and are not responsible for the observed oscillations in Sn nanoparticles. For the correction to the BCS gap equation, two types of corrections are identified, smooth and fluctuating (M.Garcia-Garcia et al. (2008); Olofsson et al. (2008)). The former depends on the surface and volume of the grain and always enhances the gap with respect to the bulk. Since this contribution decreases monotonically with the system size it is not relevant in the description of the experimental fluctuations of Δ . The self-consistent equation for the BCS order parameter in this case is (M.Garcia-Garcia et al. (2008); Olofsson et al. (2008)),

$$\Delta(\varepsilon) = \int_{-E_D}^{E_D} d\varepsilon' \frac{\lambda \Delta(\varepsilon') I(\varepsilon, \varepsilon') \nu(\varepsilon)}{2\sqrt{\varepsilon'^2 + \Delta(\varepsilon')^2} \nu(0)} \quad (2.3)$$

where $I(\varepsilon, \varepsilon') = V \int_0^L \Psi_\varepsilon^2(r) \Psi_{\varepsilon'}^2(r)$, E_D is the Debye energy, L is a typical length of the grain, $\nu(0)$ is the spectral density at the Fermi level, λ is the dimensionless coupling constant, $\nu(\varepsilon) = \sum_i g_i \delta(\varepsilon - \varepsilon_i)$ where ε_i are the eigenvalues, with degeneracy g_i , and $\psi_\varepsilon(r)$ are the eigenfunctions with energy ε of a free particle confined inside the grain. For Sn, a weak coupling superconductor a simple BCS formalism is capable of providing a good quantitative description of superconductivity. Eq. (2.3) can be further simplified by noting (M.Garcia-Garcia et al. (2008); Olofsson et al. (2008)) that for $k_F L \gg 1$ gap oscillations are controlled only by $\nu(\varepsilon)$. For L between 2-60 nm the limit is always satisfied as the Fermi wave vector $k_F = 16.4 \text{ nm}^{-1}$ in Sn. As mentioned earlier, the gap oscillations arise from the discreteness of the level spectrum (see Fig. 2) which is reflected in the

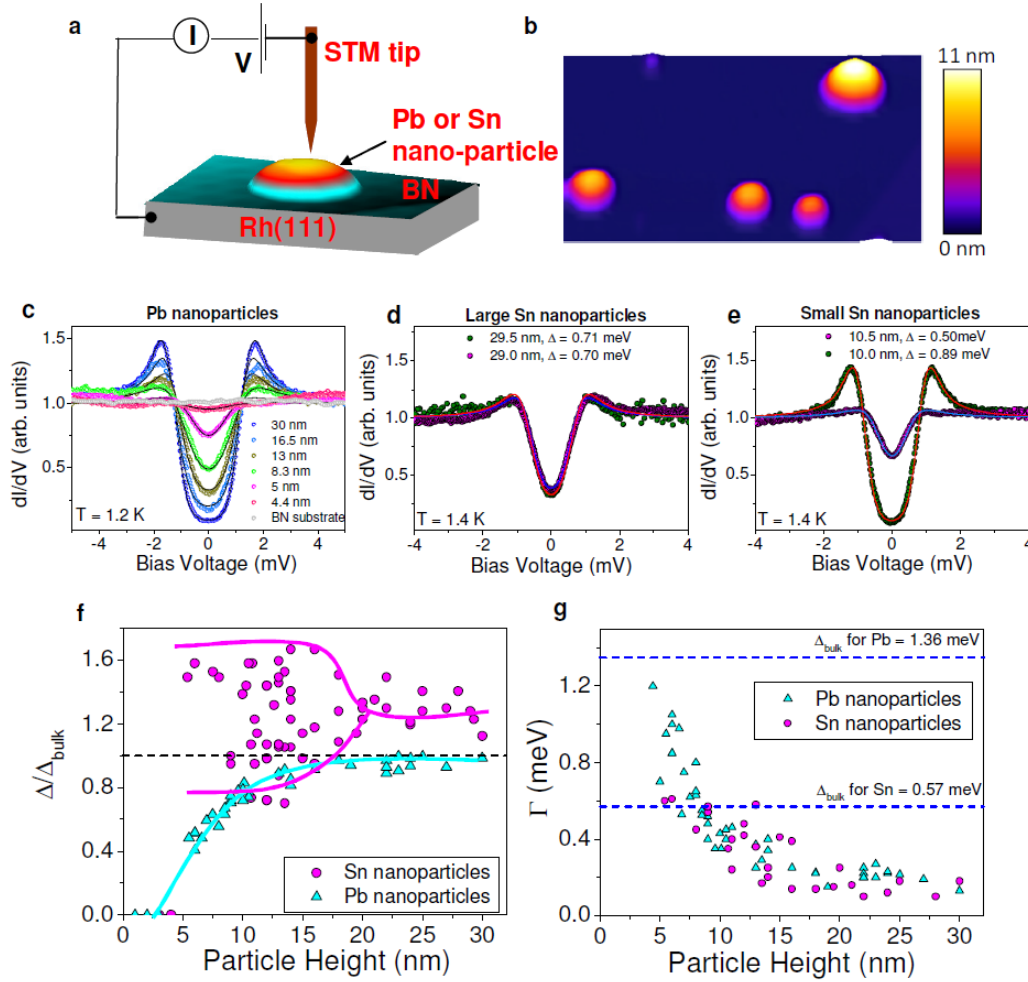


Figure 2.2: Experimental setup and low temperature superconducting properties of single, isolated Pb and Sn nanoparticles. (a) 3D representation of the experimental setup. Pb or Sn nanoparticles with height in the range 1-35 nm are deposited on a boron nitride BN/rhodium Rh (111) substrate. The investigation is done by STM measurements. (b) 125 X 90 nm² 3D STM image showing the Sn nanoparticles of varying sizes deposited on the BN/Rh (111) substrate. (c)-(e) Normalized conductance spectra (dI/dV vs V , normalized at a bias voltage of 5 mV). The circles are the raw experimental data and the solid lines are the theoretical fits using Eqns. (2.1) and (2.2). (c) Normalized conductance spectra of Pb nanoparticles of various heights at $T = 1.2$ K. (d) Normalized conductance spectra of two large Sn nanoparticles with heights 29.5 and 29.0 nm at $T = 1.4$ K. (e) Normalized conductance spectra of two small Sn nanoparticles with heights 10.5 and 10.0 nm at $T = 1.4$ K. (f) and (g) Comparison of the variation of superconducting energy gap and broadening parameter (Γ) at low temperature ($T = 1.2$ K-1.4 K) for different Pb and Sn nanoparticles respectively as a function of particle height. The gap is normalized with respect to the bulk gaps. The enhancement/decline of the superconducting energy gap is the manifestation of shell effects in Sn nanoparticles. From Ref. (Bose et al. (2010)).

expression of the spectral density $\nu(\varepsilon)$ and hence Eq. (2.3) leads to an oscillatory variation of gap with particle size. It can also be seen from the expression of $\nu(\varepsilon)$ that the presence of degeneracies ($g_i > 1$) will enhance the gap fluctuations. Large g_i is typical of grains with symmetry axes in which the energy levels are degenerate in a quantum number. A typical example is the sphere with three axes of symmetry. In this case each level in the energy spectrum with an angular momentum quantum number l is $2l + 1$ times degenerate.

An important parameter in Eq. (2.3) is λ which implies an effective coupling constant (electron-phonon coupling minus the coulomb repulsion) providing strictly within the BCS formalism a quantitative description of the superconductor. A natural choice is $\lambda = 0.25$ (for Sn) as this leads to the bulk gap and the coherence length consistent with the experimental values of these observables. The magnitude of the fluctuations will strongly depend on the shape of the grain as expected from the theory of shell effects (M.Garcia-Garcia et al. (2008)). In numerical calculations (Bose et al. (2010)) the shape of the nanoparticles has been taken as a spherical cap with $h/R > 0.85$. In the hemispherical case, $h/R = 1$, the eigenvalues are simply the roots of a Bessel function. For other ratios, the authors used a method based on a perturbative expansion around the hemispherical geometry which is only valid for $1 - h/R \ll 1$ (similar to the treatment in Ref. (Rodriguez et al. (2001))). The parameters used to describe the Sn nanoparticles are the height, h , measured by the STM, $k_F = 16.4 \text{ nm}^{-1}$, $E_F = 10.2 \text{ eV}$, $E_D = 9.5 \text{ meV}$ and the coupling constant $\lambda = 0.25$. The calculated normalized gap calculated from Eq. (2.3) is presented in Fig. 2.3a as a function of h with the superimposed experimental results of Sn nanoparticles from Fig. 2.1f (shown by solid symbols in Fig. 2.3a). Here the data is normalized with respect to the average gap value obtained experimentally. For h/R ranging between 0.9 to 0.95 a reasonably good quantitative matching with the theoretical results can be seen, indicating that finite size corrections can satisfactorily explain the results of Sn nanoparticles.

The natural question which follows is why such oscillations in Δ are not observed for Pb nanoparticles (solid triangles in Fig. 2.1f) (Note that oscillations in the gap have been observed in 2D Pb thin films below a critical thickness of 2 nm (thickness $<$ Fermi wavelength) as a function of the number of layers in the film (Ref. (Guo et al. (2004); Zhang et al. (2005); Shanenko et al. (2006a))). This phenomenon originates from the quantum confinement in the z direction leading to an oscillatory behavior of the density of states at Fermi level (with infinite degeneracy of the levels along the other two directions) and is independent of the superconducting coherence length). The fluctuations in 0D systems have its origin in the discreteness of the spectrum and any mechanism that induces level broadening will suppress these oscillations. The superconducting coherence length (ξ) of Pb ($\sim 80 \text{ nm}$) (Kittel (2004)) being much shorter than that of Sn ($\sim 240 \text{ nm}$) (Kittel (2004)) will introduce a level broadening (broadening $\propto v_F/\xi$). Moreover, since interactions are much stronger in Pb, the lifetime of the quasiparticles is shorter and an additional level broadening is expected. Fig. 2.3b presents the average oscillations obtained from both experiments and theory as a function of particle

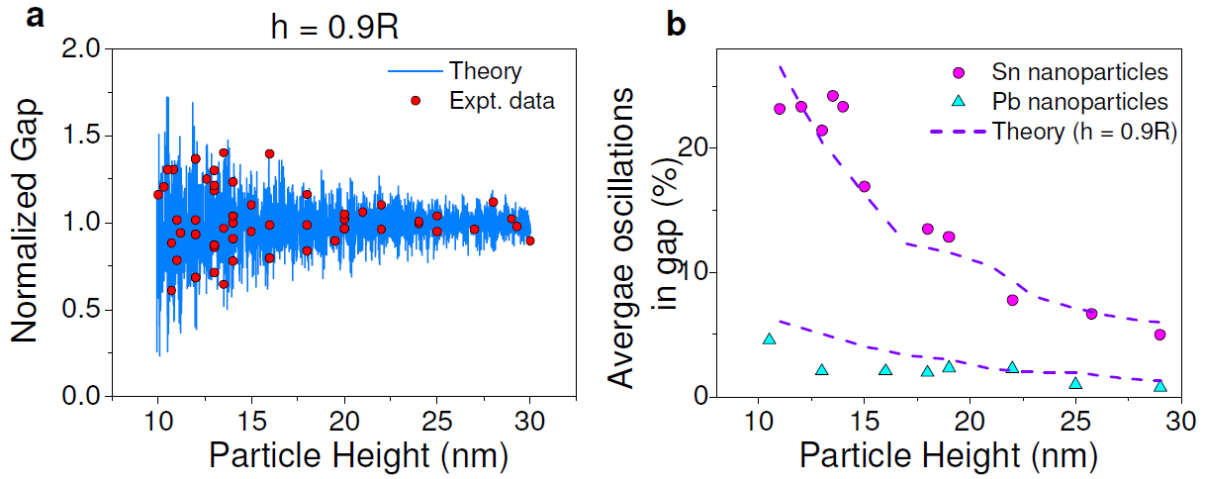


Figure 2.3: Comparison of experimental results with theoretical calculations obtained from finite size corrections to the BCS model. a, Variation of normalized gap with particle height. The solid symbols are obtained from the experimental data and the solid line is obtained from the theoretical calculations. The oscillations in the gap are explained on the basis of shell effects obtained from finite size corrections to the BCS model. b, Variation in the average oscillations in the gap for Pb and Sn with particle height. The solid symbols are experimental data while the dashed lines are obtained from the theoretical calculations. From Ref. (Bose et al. (2010)).

height for Pb and Sn nanoparticles (Bose et al. (2010)). These average oscillations are the standard deviation of the gap from the average value. A good matching between theory and experiments is observed. In order to compute the oscillations in the gap and to check the suppression of the shell effects, BCS gives a reasonably good description for the strong coupling Pb (Fig. 2.3b).

The work (Bose et al. (2010)) showed that for any classical BCS superconductor with large quantum coherence lengths it is possible to enhance the superconducting energy gap by large factors ($\sim 60\%$) by tuning only the particle size. This may prove to be very useful in case of fullerides or hexaborides which are known to show a relatively high- T_c in the bulk.

For larger clean grains, but still within the nanoscale region, numerical solutions of the the BCS gap equation (Bardeen et al. (1957)) and Bogoliubov-de Gennes equations (Parmenter (1968); Gladilin et al. (2002); Heiselberg (2003)) showed that the critical temperature and other superconducting properties were highly nonmonotonic as a function of the system size with peaks well above the bulk limit. Explicit results were obtained for a variety of shapes and confining potentials: cubes (Parmenter (1968); Gladilin et al. (2002)), spheres (Boyaci et al. (2001); Gladilin et al. (2006)), cylinders (Shanenko et al. (2006b)) and harmonic confining potentials (Heiselberg (2003)). The magnitude of the peaks, namely, the enhancement of superconductivity, was larger in spherical and cubic grains than in chaotic grains (M.Garcia-Garcia et al. (2008); Olofsson et al. (2008)) with no symmetry. Moreover, for a fixed size, deviations from the bulk limit are more pronounced as the

superconducting coherence length of the material increases. Analytical results (M.Garcia-Garcia et al. (2008); Olofsson et al. (2008)) based on the periodic orbit theory (Brack and Bhaduri (1997)) indicate that the reason for these non-monotonic deviations from the bulk limit was associated to shell effects, namely, level degeneracy in the proximities of the Fermi energy due to the geometrical symmetries of the grain. A larger spectral density induces an effective stronger binding of Cooper pairs that boost superconductivity. However, a substantial ($\approx 20\%$) monotonic enhancement of the superconducting gap up to the largest grains ≈ 30 nm studied in (Bose et al. (2010); Garcia-Garcia et al. (2011)) cannot be explained by shell effects or surface phonons. The work realized in Ref. (Mayoh and Garcia-Garcia (2013)) provide evidence that this monotonic enhancement is caused by spatial fluctuations in the density of probability of Cooper pairs in a confined geometry. The authors numerically investigated the order parameter in a hemispherical grain for sizes up to 30 nm within a mean-field framework. Using parameter free model they found a fair agreement with experimental results (Bose et al. (2010); Garcia-Garcia et al. (2011)). This additional enhancement stems from the fact that, in finite size grains, the interactions that bind the electron into a Cooper pair depend on the quantum numbers of the one-body problem eigenstates. The dimensionless electron-phonon coupling constant λ becomes inhomogeneous as it depends on these quantum numbers, $\lambda \rightarrow \lambda V I_{n,m}$ where V is the grain volume, $I_{n,m} = \int dr^d \Psi_n^2(r) \Psi_m^2(r)$ and $\Psi_n(r)$ is the eigenstate of the one-body problem and n the set of quantum numbers that labels the state. For the case of grains with no symmetry, the leading finite size correction due to this effect in Ref. (Farine et al. (2001)) is positive $I = 1 + A/k_F L$ with $A \geq 0$ that depends on boundary conditions. For a chaotic grain the semiclassical analytical analysis of Ref. (M.Garcia-Garcia et al. (2008)) showed that this the leading correction for sizes $L \geq 10$ nm.

The superconducting grain is described by the BCS Hamiltonian (Bardeen et al. (1957)),

$$H = \sum_{\mathbf{n}\sigma} \epsilon_{\mathbf{n}} c_{\mathbf{n}\sigma}^\dagger c_{\mathbf{n}\sigma} - \frac{\lambda}{\nu(0)} \sum_{\mathbf{n}, \mathbf{n}'} I_{\mathbf{n}, \mathbf{n}'} c_{\mathbf{n}\uparrow}^\dagger c_{\mathbf{n}\downarrow}^\dagger c_{\mathbf{n}'\uparrow} c_{\mathbf{n}'\downarrow} \quad (2.4)$$

where $c_{\mathbf{n}\sigma}^\dagger$ creates an electron of spin σ in a state with quantum numbers \mathbf{n} and energy $\epsilon_{\mathbf{n}}$, λ is the dimensionless BCS coupling constant for the material, $\nu(0)$ is the density of states at the Fermi energy. The electron-electron interaction matrix elements resulting from a contact interaction is given by,

$$I_{\mathbf{n}, \mathbf{n}'} = V \int \psi_{\mathbf{n}}^2(\mathbf{r}) \psi_{\mathbf{n}'}^2(\mathbf{r}) d\mathbf{V} \quad (2.5)$$

where V is the volume of the grain and $\psi_{\mathbf{n}}(r)$ is single-electron eigenfunction in state \mathbf{n} . The superconducting gap is calculated from the self-consistency equation,

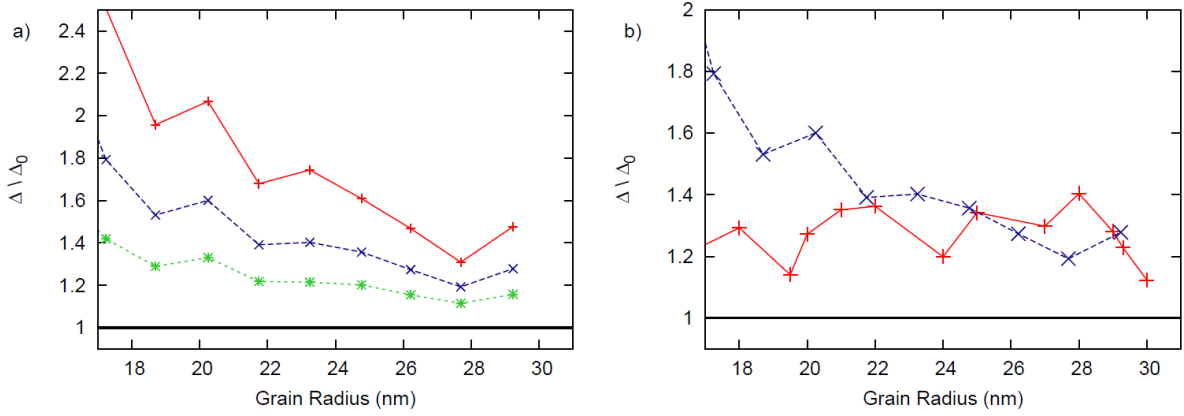


Figure 2.4: (a) The mean superconducting gap as a function of the hemispherical grain size for $\lambda = 0.166$ Al (dotted line), $\lambda = 0.243$ Sn (dashed line), $\lambda = 0.382$ Pb (solid line). (b) Comparison between the experimental results (solid line) of Ref. (Bose et al. (2010); Garcia-Garcia et al. (2011)) for Sn hemispherical nanograins and the theoretical prediction (dashed line) Eq.(5) that includes the effect of inhomogeneous pairing. The fluctuations are averaged in order to single out the contribution not related to shell effects in the spectral density. The horizontal line corresponds to the bulk behavior. From Ref. (Mayoh and Garcia-Garcia (2013)).

$$\Delta_n = \frac{\lambda}{2} \sum_{n'} \frac{\Delta_{n'} I_{n,n'}}{\sqrt{\epsilon_{n'}^2 + \Delta_{n'}^2}} \frac{1}{\nu(0)} \quad (2.6)$$

where the sum is now taken over all states $\{n' \mid |\epsilon_{n'}| < \epsilon_D\}$, and ϵ_D is the Debye energy. It should be noted that this approach leads to results similar to those obtained from the technically more involved Bogoliubov-de Gennes equations (Croitoru et al. (2011)). In the bulk limit eigenfunctions are plane waves and the matrix elements are simply $I_{n,n'} = 1$. However, in small grains eigenstates of the one-body problem are not plane waves so the deviations are expected in $I_{n,n'}$ from the bulk limit. The BCS mean field approach is valid for grains such that $\delta/\Delta_0 \ll 1$. In order to make direct comparison with experimental results authors calculated numerically $I_{n,n'}$ for hemispherical grains of radius R (Mayoh and Garcia-Garcia (2013)). Because the experimental grains are not exactly hemispherical but closer to a spherical cap of height $h \sim 0.9R$ (Bose et al. (2010); Garcia-Garcia et al. (2011)). The eigenfunctions entering in the matrix element above are those of a single electron in a spherical grain of radius R ,

$$\psi_{n,l,m}(r, \theta, \phi) = N j_l \left(u_{ln} \frac{r}{R} \right) Y_{lm}(\theta, \phi) \quad (2.7)$$

where $N = 2/(j_{a+1}(u_{am})R^{3/2})$ is the normalisation constant, $j_l(r)$ are the spherical Bessel functions of the first kind, u_{ln} is the n^{th} zero of the l^{th} spherical Bessel function and $Y_{lm}(\theta, \phi)$ are the

spherical harmonics. The energy associated with these eigenstates is, $E_{l,n} = \hbar^2 u_{ln}^2 / 2mR^2$. Dirichlet boundary conditions on the hemispherical surface (Rodriguez et al. (2001)) restricts $|m - l|$ to be odd. The final expression for the matrix elements is simplified by using Clebsch-Gordan coefficients,

$$I_{n,n'} = \frac{4(2l+1)(2l'+1)}{3j_{a+1}(u_{am})^2 j_{a'+1}(u_{a'm'})^2} \sum_{\Lambda} \frac{\langle ll', mm' | ll', \Lambda M \rangle^2 \langle ll', 00 | ll', \Lambda 0 \rangle^2}{2\Lambda + 1} \quad (2.8)$$

$$\times \int_0^1 j_l(u_{ln}\rho)^2 j_{l'}(u_{l'n'}\rho)^2 \rho^2 d\rho \quad (2.9)$$

where $M = m + m'$ and Λ is summed over all possible values in the range, $l + l' \geq \Lambda$, $|l - l'| \leq \Lambda$ and $m \leq |\Lambda|$. The superconducting gap can then be written as,

$$\Delta = 2\epsilon_D e^{-\frac{1}{\lambda_{eff}}} \quad (2.10)$$

where $\lambda_{eff} = \lambda \bar{I}$ and \bar{I} is the average of $I_{n,n'}$ over all states in the interacting region $2\epsilon_D$ where n' is the level closest to the Fermi-energy. This should be a good approximation for sufficiently large grains for which the matrix elements do not depend strongly on the quantum numbers. This is also consistent with the observation that in scanning tunnelling microscope experiments (Bose et al. (2010); Garcia-Garcia et al. (2011)) the value of the gap did not depend much on the exact position of the tip. Moreover it was found in Ref. (M.Garcia-Garcia et al. (2008)) that a similar simplified expression for the gap describes shell effects related to fluctuations of the spectral density. In that case the resulting spectral density after solving the gap equation is expressed as a finite sum over classical periodic orbits of length less than the superconducting coherence length. Calculations with $\lambda = 0.243$ is consistent with the Sn bulk gap $\Delta_{bulk} = 0.57$ meV and a Debye energy $\epsilon_D = 17.2$ meV. The numerical results in Fig. 2.4 (Mayoh and Garcia-Garcia (2013)) show substantial deviations from the bulk even at large grain sizes. The theoretical prediction is strikingly similar to the experimental observation. Fig. 2.4 shows similar results for other materials. From Eq. (2.10) it is clear that finite size effects are stronger the smaller is the coupling constant λ . In more physical terms, finite size effects are stronger in materials with a long superconducting coherence length $\xi \propto 1/\Delta \propto e^{1/\lambda}$. The deviations for smaller sizes < 18 nm are likely due to the difference between the spherical cap shape of the experimental grains and the exact hemispherical shape employed in the theoretical calculation.

Enhancement of superconductivity by engineered nanogranularity

Experimental reports, starting in the sixties (Abeles et al. (1966); Giaever and Zeller (1968)), of substantial enhancement of superconductivity in thin granular films of different materials have been a continuous stimulus to study superconductivity in low dimensions. However, the dramatic increase of the critical temperature observed in materials like Al or Sn (Abeles et al. (1966); Giaever and Zeller (1968)) resisted a conclusive theoretical explanation. The cause of the enhancement was related to surface phonons, fluctuations of the spectral density around the Fermi energy or shape resonances (Blatt and Thompson (1963); Thompson and Blatt (1963); Perali et al. (1996)). The first two proposals could not be reconciled with the fact that the enhancement was observed on some materials but not in others. The latter mechanism, put forward by Blatt and Thompson (Blatt and Thompson (1963); Thompson and Blatt (1963)), is only effective for clean thin films with only a few monolayers thick. However, the samples were granular and disordered. Indeed, more refined experimental studies (Haviland et al. (1989); Guo et al. (2004)) where thin films were smoother and granularity was attenuated showed no substantial enhancement of superconductivity.

Investigation in Ref. (Mayoh and Garcia-Garcia (2014b)) showed that size effects can also enhance the critical temperature of a bulk granular material composed of such nanograins. They have studied a three dimensional array as global phase-coherence is easier to achieve in higher dimensionalities and a mean-field approach is more accurate. The grain size in a realistic array (Bose et al. (2010); Eley et al. (2012)) varies substantially so a random distribution of sizes is a good description of the experimental situation. This implies only some grains have a T_c higher than that of the bulk material, T_{c0} . The number of grains with $T_c > T_{c0}$ increases as the array resistance decreases due to the suppression of shell effects. At the same time the maximum T_c in a single grain increases as the resistance increases. Percolation theory is a useful tool in the search for the optimal compromise between these two competing effects. The mean-field Bardeen-Cooper-Schrieffer formalism and semi-classical techniques are only applicable when $k_F R \gg 1$ and $T_{c0} \gg \delta$ so that thermal and quantum fluctuations are negligible, where k_F is the Fermi-wave vector and R is the radius of the

grain. Typically this limit corresponds to $R \geq 5$ nm though the exact value depends on the material. The model considered in Ref. (Mayoh and Garcia-Garcia (2014b)) employed the coupling of a single grain to the rest of the array using semiclassical techniques and a mean- field formalism. The overall effect of the coupling is a smoothing of the density of states that suppresses finite size effects. Superconductivity in each grain is described by the BCS (Bardeen et al. (1957)) Hamiltonian,

$$H = \sum_{n\sigma} \epsilon_n c_{n\sigma}^\dagger c_{n\sigma} - \frac{\lambda}{\nu_{TF}(0)} \sum_{n,n'} I_{n,n'} c_{n\uparrow}^\dagger c_{n\downarrow}^\dagger c_{n'\uparrow} c_{n'\downarrow} \quad (3.1)$$

where $c_{n\sigma}^\dagger$ creates an electron of spin σ in state n with energy ϵ_n , λ is the dimensionless BCS coupling constant, $\nu_{TF}(0)$ is the bulk density of states at the Fermi energy, ϵ_F , and $I_{n,n'}$ are the short range electron-electron interaction matrix elements. The second sum is taken over all of the states within the Debye energy, ϵ_D , window around ϵ_F . The superconducting gap $\Delta(R, T)$ is given by,

$$1 = \frac{\lambda}{2} \int_{-\epsilon_D}^{\epsilon_D} \frac{1}{\sqrt{\epsilon'^2 + \Delta^2}} \frac{\nu(\epsilon')}{\nu_{TF}(0)} \tanh\left(\frac{\beta\sqrt{\epsilon'^2 + \Delta^2}}{2}\right) d\epsilon' \quad (3.2)$$

where $\beta = 1/k_B T$ and $\nu(\epsilon) = \sum_n \delta(\epsilon - \epsilon_n)$ is the exact single particle density of states. Here $\nu(\epsilon)$ is dependent on the size of the grain and is the parameter responsible for including size effects in the model. The most important difference between an isolated grain and one coupled to an array is that in the latter quasiparticles can escape by tunneling. The grain is therefore open and its density of states is smoothed. This smoothing is modeled by expressing the density of states analytically as a sum over classical periodic orbits with a cut-off that depends on the probability of intergrain tunneling (Mayoh and Garcia-Garcia (2014b)). The intergrain tunneling is a function of the tunneling resistance of the junction R_N and the number of nearest neighbor. Explicit expressions for $T_c(R)$ and $\Delta(R, T = 0)$ as a function of the grain radius R are then obtained from Eq. (3.2) by a power expansion in the small parameter $(k_F R)^{-1/2}$ (Garcia-Garcia et al. (2011)). The superconducting gap close to T_c is given by,

$$\Delta(R, T) \approx 1.74\Delta(R, 0) \sqrt{1 - \frac{T}{T_c(R)}}. \quad (3.3)$$

In order to mimic realistic experimental conditions (Bose et al. (2010); Deutscher et al. (1973); Shapira and Deutscher (1982)) the authors considered a Gaussian distribution of grain sizes, $P(R)$, with mean \bar{R} and standard deviation σ (Mayoh and Garcia-Garcia (2014b)). As a consequence T_c and the gap Δ are different in each grain. The fraction of grains in the normal metal phase increases as temperature increases. For a three dimensional array a Kosterlitz-Thouless transition (Kosterlitz and Thouless (1973)) is not favorable since, even close to the percolation threshold, the dimen-

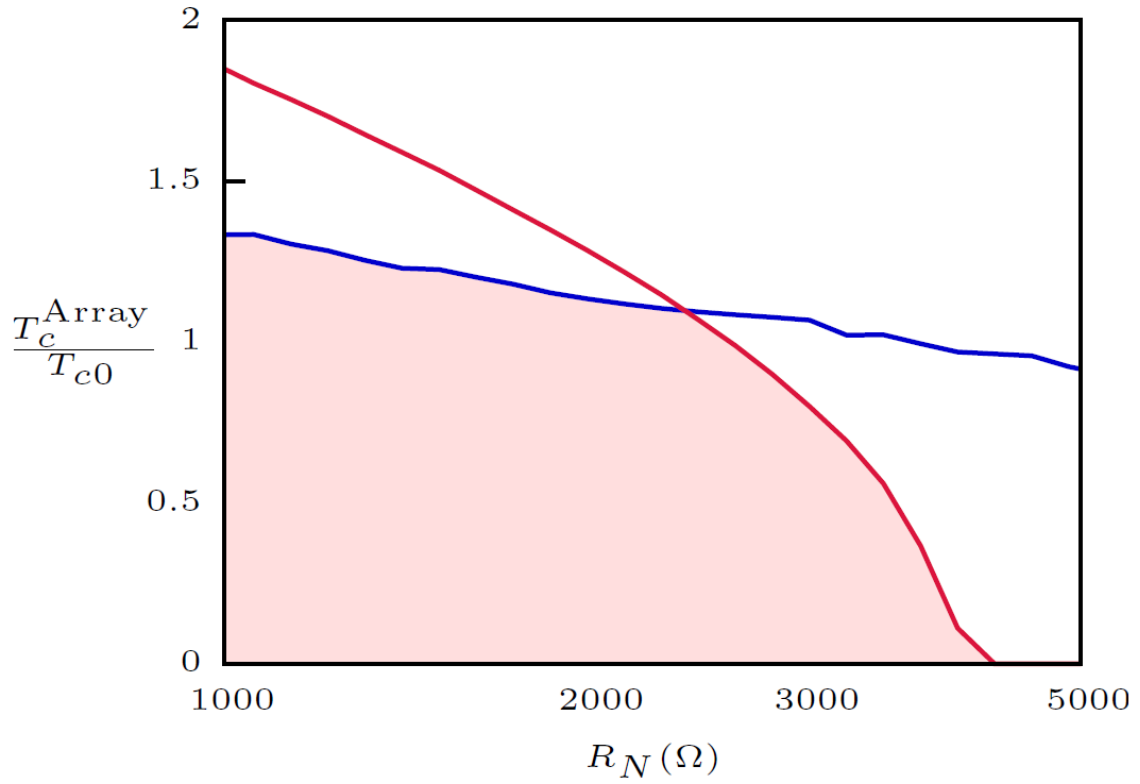


Figure 3.1: The critical temperature of the array in units of the bulk critical temperature of the material against R_N for a cubic array with $\epsilon_F = 10.2$ eV, $\epsilon_D = 9.5$ meV, $\bar{R} = 5$ nm, $\sigma = 1.0$ nm and $\lambda = 0.3$. The blue line shows the critical temperature due to percolation given by finding the temperature at which $p = p_c$. The red line shows the critical temperature due to phase-fluctuations. Close to 2.5 k Ω these two lines cross meaning the transition that breaks global-phase coherence goes from being percolation to phase-fluctuation driven. The shaded region shows the range of parameters for which the array will be globally superconducting. This cross-over corresponds to the sharp tail seen at large resistance in the following figures. From Ref. (Mayoh and Garcia-Garcia (2014b)).

sionality of the percolating cluster is $D_f \sim 2.52 > 2$ (Ballesteros et al. (1999)). The grains that belong to the superconducting cluster are those that verify $T_c(R) \geq T_c^{\text{Array}}$, they have a distribution $P_{sc}(R) = \Theta(T_c(T) - T)P(R)$. There are two distinct ways to destroy global phase-coherence in the array. First, the array may reach its percolation threshold $p = p_c$ where p is the fraction of grains in the superconducting phase, $p = \int_0^\infty P_{sc}(R)dR$, and p_c is the percolation threshold of the array. Beyond the percolation threshold there may exist globally phase-coherent clusters but these do not permeate the whole array. Second, global phase-coherence may be destroyed by phase fluctuations. In the former the critical temperature is defined as the temperature for which the number of grains still superconducting, computed using the expressions obtained previously, form the critical percolating cluster. The calculation of the latter requires a more elaborate treatment. For this type of array (Chakravarty et al. (1987)) the action includes charging effects, quasiparticle tunneling and the Josephson coupling, which is highly inhomogeneous as the value of the superconducting gap is different in each grain.

The position dependence of the Josephson coupling term can be removed by expressing it in terms of the mean gap $\bar{\Delta}_{ij} = (\Delta_i + \Delta_j)/2$ and the difference in the gaps $\Delta'_{ij} = (\Delta_i - \Delta_j)/2$ across the junction and expand in powers of Δ'_{ij} . The superconducting cluster can be expressed by a homogeneous array with $\bar{\Delta}_{ij}$ replaced by the mean value for the cluster, $\bar{\Delta} = 1/p^2 \int_0^\infty \int_0^\infty (\Delta(R) + \Delta(R'))/2 P_{sc}(R)P_{sc}(R')dRdR'$. A similar procedure is applied to Δ'_{ij} . This is a good approximation as close to T_c^{Array} the distribution of $\bar{\Delta}_{ij}$ and Δ'_{ij} in the cluster will be narrow and sharply peaked around this value. The mean number of superconducting neighbor grains in the percolating cluster, $\bar{z} = zp$, slightly underestimates the coordination number of the infinite cluster as this is the mean coordination number for the whole array including both finite clusters and the infinite cluster, however this discrepancy is small.

The resulting homogeneous action (Panyukov and Zaikin (1987)) can be tackled by standard mean-field techniques. The critical temperature of the array, due to phase-fluctuations, is obtained by finding the solution to,

$$1 = \frac{\tilde{E}_Q}{\bar{z}J} + e^{-\beta\tilde{E}_Q/2} \quad (3.4)$$

where $\tilde{E}_Q = (1/E_Q + \eta/E_Q^*)^{-1}$, $E_Q^* = 124e^2\bar{\Delta}R_N/3\pi\hbar$, $J = \bar{\Delta}R_Q/2R_N \tanh(\beta\bar{\Delta}/2) - \Lambda$. The critical temperature of the array, T_c^{Array} can be defined to be the lower of the two critical temperatures. The theoretical treatment assumes (Mayoh and Garcia-Garcia (2014b)) that intergrain coupling is constant however the distance between grains in realistic arrays is rather random but with a well defined average and small variance. The random coupling only affects the percolation transition through the weakening of size effects in single grains which is a small correction. The random couplings will lower the critical temperature of the array with regard to phase-fluctuation. However, this should not affect the maximum of the critical temperature which occur far from the quantum

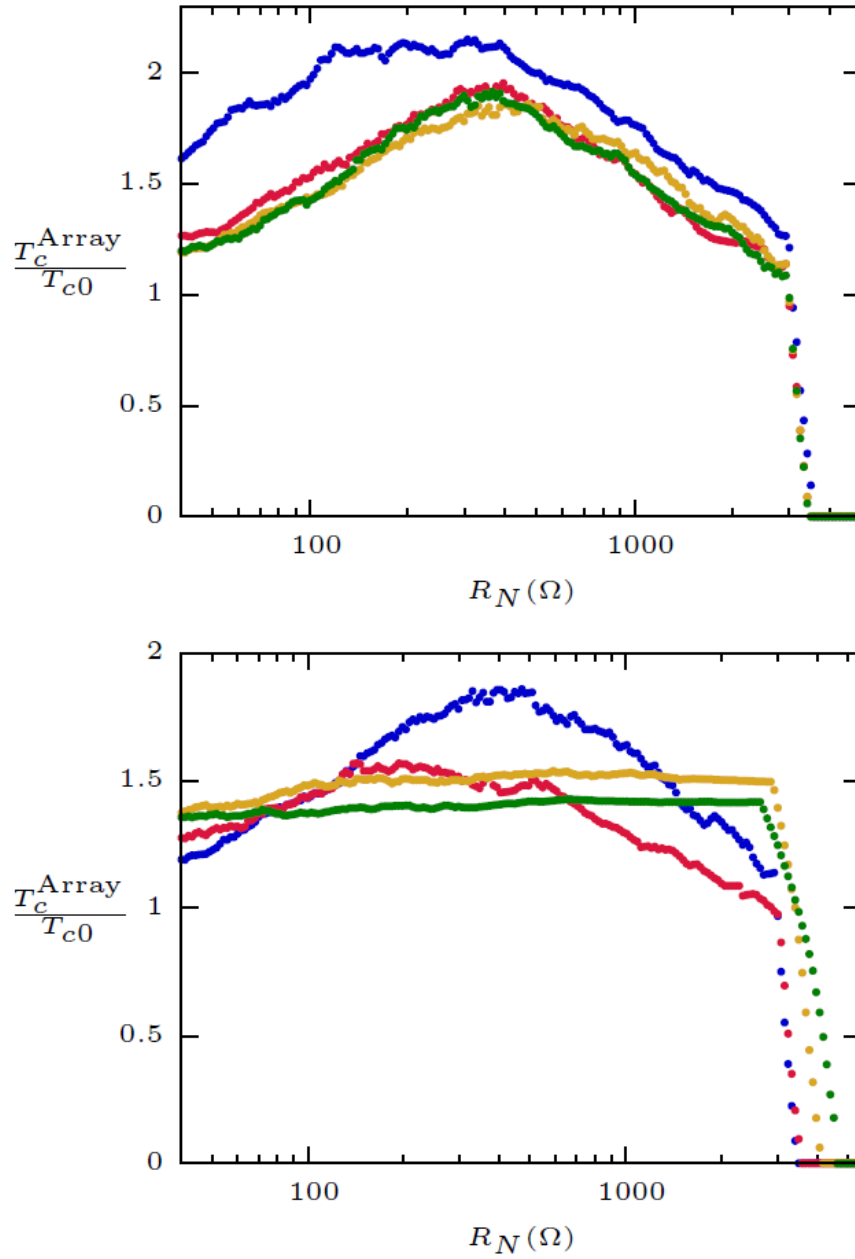


Figure 3.2: T_c^{Array} in units of the bulk material critical temperature, against R_N for a cubic array with $\epsilon_F = 10.2$ eV, $\epsilon_D = 9.5$ meV, $\lambda = 0.25$. Top: Gaussian distribution of sizes with mean $\bar{R} = 5$ nm, and variance $\sigma = 0.1$ nm (blue, solid), 0.6 nm (red), 1.0 nm (yellow) and 1.4 nm (green). Results are weakly dependent on σ (for $\sigma > 1$ Å) as the typical scale for which shell effects in the size distribution are not randomized is much smaller. Bottom: $\sigma = 1.0$ nm and $\bar{R} = 5$ nm (blue), 7 nm (red), 11 nm (yellow), 17 nm (green). T_c^{Array} becomes independent of R_N , due to the decreasing importance of quasiparticle tunnelling, and then gradually decreases for increasing \bar{R} due to the weakening of shell effects. From Ref. [(Mayoh and Garcia-Garcia (2014b))].

resistance where phase-fluctuations are important.

The computation of T_c^{Array} in Ref. (Mayoh and Garcia-Garcia (2014b)) had an assumption that the grain size distribution is a Gaussian, $P(R) = 1/(\sqrt{2\pi}\sigma)e^{-(R-\bar{R})^2/(2\sigma^2)}$. This choice with $\sigma \sim 1$ nm and $\bar{R} \sim 5$ nm is a good approximation to the experimental distribution (Deutscher et al. (1973); Shapira and Deutscher (1982)), with $C = 4\pi\epsilon_0 R \sim 0.5aF$. However, this capacitance is typically strongly renormalized by the quasiparticle tunneling so its value does not influence the results. Fig. 3.1 depicts both critical temperatures for typical values of the grain size and tunneling resistance. A percolation driven transition is observed for $R_N \lesssim R_Q$. For larger R_N phase fluctuations, induced by \tilde{E}_Q , break long range order at temperatures below the percolation transition.

For experimentally realistic values the results depend very weakly on σ , see Fig. 3.2. This is expected as oscillations in the order parameter due to shell effects take place on a much smaller length scale ~ 1 Å. Indeed, when σ is tuned to this range substantial deviations appear depending on whether shell effects enhance or suppress $T_c(R)$ for $R = \bar{R}$.

In Fig. 3.2 the T_c^{Array} has a peak at ~ 500 Ω indicating there is an optimal coupling strength for the array. In general, an increase in T_c^{Array} is expected as R_N increases due to the decreasing strength of intergrain coupling. This makes the shell effects within each grain larger meaning some grains now have a significantly enhanced T_c . However, for sufficiently large $R_N \lesssim R_Q$ there is very little smoothing of the spectral density in single grains. This results in a lower T_c^{Array} as the fraction of grains with an enhanced T_c is not sufficient to form a percolating cluster. This is the reason for the peak observed at intermediate R_N .

For large mean grain size, \bar{R} , results should be less dependent on R_N as in this case the width of the peaks in the density of states is not controlled by R_N but rather by the coherence length $\xi = \hbar v_F / \Delta_0$. Finite size effects diminish as \bar{R} increases which results in a smaller enhancement of T_c^{Array} as the T_c of the single grains is not increased as much, as can be seen in Fig. 3.2. The restriction to $\bar{R} > 5$ nm reduces influence of thermal and quantum fluctuations, that break the mean-field theory approach, making them unimportant. For a broad range of \bar{R} , T_c^{Array} is well above that of a non-granular bulk material. This is a quite general result that only requires a three dimensional array is inhomogeneous with a distribution of $T_c(R)$ around the bulk value T_{c0} . The value of the BCS coupling constant, λ , also plays an important role in T_c^{Array} . The larger λ , the less important size effects are. This follows from the fact that the coherence length ξ decreases as λ increases thus making the material more bulk like. This prevents the employment of the BCS theory based approach in the study of cuprates and other strongly coupled superconductors. The results presented in Fig. 3.3 fully confirm this picture. Strikingly the array geometry, the way spheres are packed in the array, has a substantial effect on T_c^{Array} .

Settings which decrease the percolation threshold allow the array to remain globally phase-coherent with fewer superconducting grains. This results in a much higher T_c^{Array} , observable in Fig. 3.3.

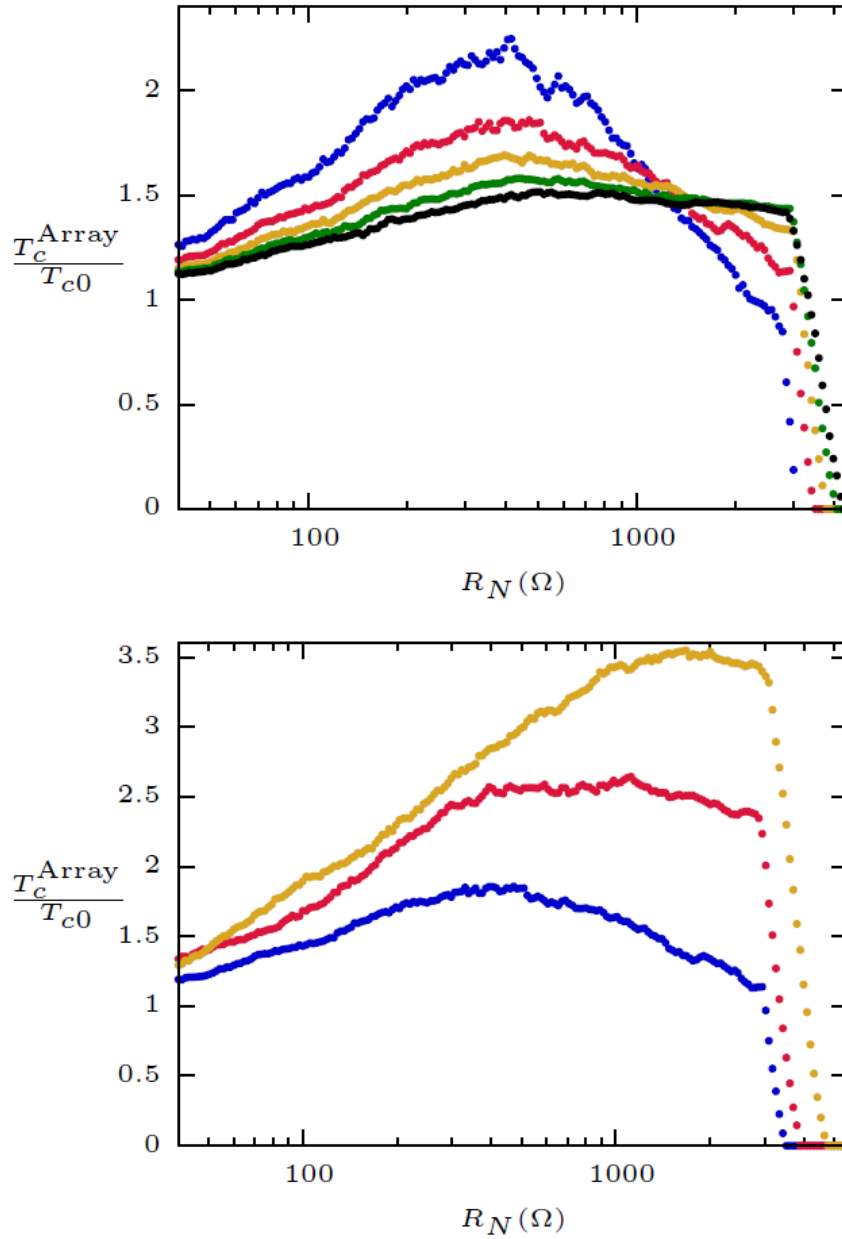


Figure 3.3: T_c^{Array} in units of the bulk material critical temperature against R_N with $\epsilon_F = 10.2$ eV, $\epsilon_D = 9.5$ meV, $\bar{R} = 5$ nm, $\sigma = 1.0$ nm. Top: A cubic array with $\lambda = 0.2$ (blue), 0.25 (red), 0.3 (yellow), 0.35 (green), 0.40 (black). Increasing λ suppress size effects resulting in a behavior which is closer to the bulk. Bottom: $\lambda = 0.25$ for a cubic (blue), BCC (red) and FCC (yellow) array. A smaller p_c substantially enhances T_c^{Array} by allowing the removal of more grains from the superconducting cluster so that the remaining ones have a higher T_c . From Ref. [(Mayoh and Garcia-Garcia (2014b))].

The peaks for intermediate R_N also moves to larger values of the resistance since the coupling between grains becomes stronger with increasing z . The outcome of this detailed analysis is that the maximum increase of T_c^{Array} , with respect to the bulk limit, is found in arrays of weakly coupled superconductor, $\lambda \ll 1$ with a mean grain size ~ 5 nm, for intermediate resistances and for packings with a minimal percolation threshold.

Phase fluctuations and shell effects in Indium nanocomposites

For many years the role of disorder in superconductivity was believed to be well understood. According to the Anderson theorem (Anderson (1959)), weak non-magnetic impurity scattering does not influence the critical temperature of a conventional weakly-coupled superconductor. These results are based on the assumption that the local density of states in the material is unaffected by weak disorder (Kim and Overhauser (1993)). However with the development of the Bogoliubov-de Gennes theory of superconductivity (de Gennes (1964)) it became clear that the order parameter becomes increasingly inhomogeneous with increasing disorder. Over the past few decades, it has been realized that the ground state in conventional superconductors is affected by disorder, resulting in unusual metallic and insulating states (Goldman and Markovic (1998)). However, recent experiments indicate that even after the global superconductivity is destroyed, the material continues to manifest some of the superconducting fundamental properties. For example, the observation of magnetic flux quantization in disordered insulating Bi films (Stewart et al. (2007)), finite high-frequency superfluid stiffness above T_c in amorphous InO_x films (Crane et al. (2007)), and the formation of a pseudogap above T_c (Sacepe et al. (2008)). Theoretical investigations also indicate that strong superconducting correlation can persist even after global superconductivity is destroyed (Feigel'man et al. (2007)).

The superconducting state is characterized by a complex order parameter of the form $\Psi = |\Delta|e^{i\phi}$. There are three kinds of excitations that can destroy the superconducting state. First of all, it is quasiparticle excitations which influencing the amplitude Δ . Second, quantum phase fluctuations connected to the number-phase uncertainty relation. And the third one is the classical phase fluctuations produced by thermal excitations. The BCS and Eliashberg mean-field theories (Tinkham (1996)) are well suited for description of the clean conventional superconductors where quasiparticle excitations are of great importance (Emery and Kivelson (1995)). In the case of strongly disordered superconductors, the screening of the Coulomb interactions is poor (Anderson et al. (1983)) and the superfluid density (n_s) is small due to disorder scattering (Tinkham (1996)). These considerations

make the disordered systems sensitive to phase fluctuations. Strong phase fluctuations can completely suppress the superconductivity. Numerical calculations also show that the superconducting state can get destroyed by strong phase fluctuations between domains that emerge in the presence of strong disorder (Dubi et al. (2007)). At the same time, experimental evidence that phase fluctuations play a central role in the formation of a pseudogap state in a disordered s -wave superconductor has been observed by Mondal *et al* (Mondal et al. (2011)). Close to critical disorder, a finite gap in the electronic spectrum even at temperatures well above T_c has been observed. The superfluid density is strongly suppressed at low temperatures and aims to a linear temperature dependence at higher temperatures (Mondal et al. (2011)).

Numerical investigations of strongly disordered superconductors by Bogoliubov-de Gennes approach shows compelling evidence for the shell-like effect (Ghosh and Mandal (2013)). The occurrence of the effects can emerge from the inhomogeneity of the nanosize granular structures inside strongly disordered superconductors. As is explained in Chapter 3, superconductivity in the array of nanogranulars is enhanced by the shell effects of the single grains and overall critical temperature is determined by tunnelling resistance.

Superconducting nanocomposites are interesting objects for investigations because of the interconnection between phase fluctuations and shell effects. By changing the size of the bridges between the granules one can create disorder in the system which leads to phase fluctuations and increase of resistance. At the same time the local critical temperature of the granule is also dependent on tunnelling resistance due to shell effects. Depending on the structure, disorder can be introduced in both correlated and uncorrelated ways for opal and porous glass systems, respectively.

4.1 Sample characterization

In this Chapter the results for superconducting Indium-opal and porous glass samples are presented and discussed.

Opal is a densely packed, face-centered cubic array of identical silicate spheres (Bogomolov et al. (1987)) with voids between contacting spheres. The FCC packing of spheres of diameter D has two types of voids. The O voids are octahedral with a characteristic size $d_O = 0.41D$. The T voids are tetrahedral with characteristic diameter $d_T = 0.23D$. The O and T voids interconnected by channels of varying cross section with the smallest size $d_b = 0.15D$. Voids in the opal form a regular lattice. In the present work, opals with spheres of different size are discussed. Their physical dimensions and characteristics are presented in Table 4.1, The scatter in diameter is less than 5% for each sample. The void dimensions has been altered by the method of molecular layer-by-layer deposition of oxides on the inner surface of the silica gel (Romanov et al. (1993); D. V. Shamshur and Romanov (2000)). Hence, the diameter of the indium granules has been changed within the thickness of one molecular layer of the deposited oxide. One operational cycle including several chemical reactions

applies one monatomic TiO_2 layer. The opals discussed in the work have different numbers of titanium oxide monolayers (up to 60). Another route of changing the indium volume in opal is the deposition of a thick SiO_2 layer from a polysilicate solution on the inner opal surface. This method has been incorporated in samples 1.3 and 1.4, see Table 4.1 for details. In those cases, the free volume fraction of opal voids f has been reduced considerably, from 26% in an ideal fcc lattice to 13%. In order to prepare an indium–opal nanocomposite, molten In metal has been injected into the voids of the opal samples by pressure (Bogomolov et al. (1982)). The geometry of the studied samples is about $5 \times 2 \times 0.4$ mm.

Table 4.1: Geometric characteristics and superconducting transition parameters of the In–opal nanocomposites studied. The explanation of the designation is given in the text.

Sample	f_{In}	N_{TiO_2}	δ , nm	D , nm	d_O , nm	d_T , nm	d_b , nm	T_c , K	$H_{c2}(0)$, Oe
1.1	0.26	0	0	230	95	52	36	3.57	2200
1.2	0.17	54	7.2	230	81	37	21	3.66	3850
1.3	0.08	34	13	230	69	26	10	3.72 - 4.17	18900 - 22200
1.4	0.13	0	8.2	230	79	35	19	4.15	15000
2.1	0.26	0	0	290	120	66	45	3.49	940
2.2	0.22	20	2.7	290	115	60	40	3.495	1250
2.3	0.19	40	5.3	290	109	55	34	3.51	1750
2.4	0.16	60	8.0	290	104	49	29	3 - 5	2200 - 5000

The electron-microscope picture of one of the indium–opal samples is presented in Fig. 4.1. As follows from the SEM image, indium metal forms a regular continuous three-dimensional network between the dielectric spheres. If one looks at the cross section of the material, it is seen that indium network is a regular array of closed contours interconnected by bridges with smaller size. The metal fills the entire opal free space (Tretyakov et al. (1998); Balakirev et al. (1993)), and, therefore, the metal network is a spatial replica of the sphere array.

To eliminate the presence of surface conductivity, indium has been removed from the surface region of the opal by etching it in a 20% solution of nitric acid for 20 min. After the etching process the absence of surface conductivity of the sample has been confirmed. And only then contact pads less than 0.3 mm wide have been prepared by grinding. Thereafter these pads have been filled with a current-conducting glue-based silver paste.

Experimental data is presented for indium–opal samples of two lots. The difference between the two groups is in the diameter of the silicate spheres which constitute the opal matrix. The characteristic geometric dimensions of the opal voids and the superconducting transition parameters of the nanocomposite samples studied are listed in Table 4.1. Also the number of TiO_2 layer deposition cycles, the oxide thickness δ , and the indium volume fraction f_{In} are provided in Table 4.1.

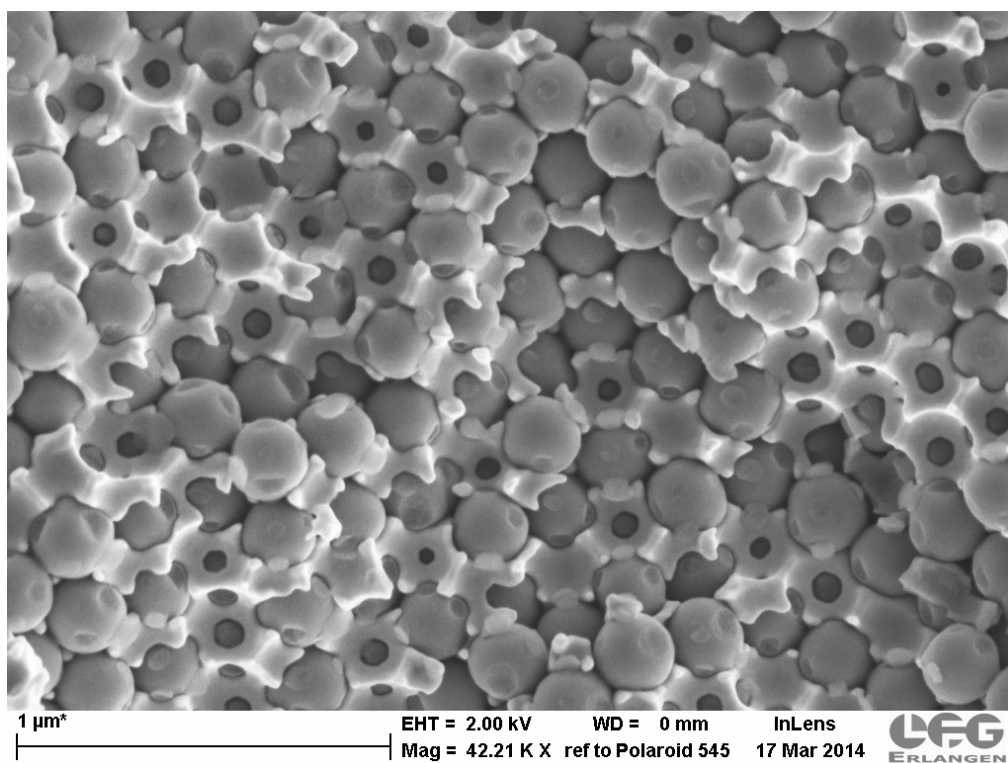


Figure 4.1: SEM image of In-opal surface.

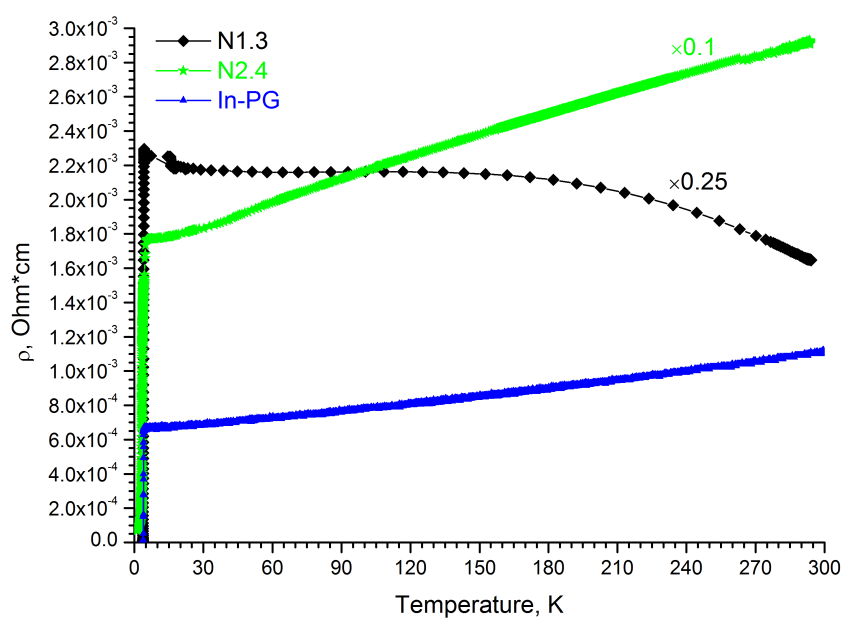


Figure 4.2: Temperature dependences of resistivity of In-opal samples 1.3, 2.4, and In-porous glass.

Table 4.2: Electrical resistivity of the In network.

Sample	$\rho_s(300 \text{ K}), \text{ m}\Omega\cdot\text{cm}$	$\rho_s(4.2 \text{ K}), \text{ m}\Omega\cdot\text{cm}$	$\frac{\rho_s(300 \text{ K})}{\rho_s(4.2 \text{ K})}$
1.1	0.066	0.009	7.41
1.2	0.101	0.035	2.9
1.3	>0.102	0.138	0.74
1.4	0.455	0.257	1.77
2.1	0.058	0.004	14.32
2.2	0.057	0.008	7.11
2.3	0.065	0.012	5.54
2.4	>0.08	0.042	1.91

In order to define the geometric dimensions of indium nanoparticles, the shape of each grain has been approximated by a sphere with diameter equal to the opal void diameter reduced by 2δ to account for the thickness of the TiO_2 layers.

$$d_O = D(\sqrt{2} - 1) - 2\delta, \quad d_T = D\left(\sqrt{\frac{3}{2}} - 1\right) - 2\delta, \quad d_b = D\left(\frac{2}{\sqrt{3}} - 1\right) - 2\delta. \quad (4.1)$$

The indium bridges interconnecting the grains are elongated by the TiO_2 overgrowing procedure. Hence, it is natural to approximate these by the cylinders. The cylinder axis length is

$$L = D\left(1 - \frac{\sqrt{2}}{2}\right) + 2\delta. \quad (4.2)$$

The dimensions of indium nanoparticles d_O , d_T , and d_b have been determined by two different methods, which depends on the approach employed to calculate the total TiO_2 layer thickness. In one method, the relation $\delta = N_{\text{TiO}_2}\delta_1$ has been used, where $\delta \approx 0.13 \text{ nm}$ is the monolayer thickness derived with due account of the anatase structure. The other method is based on optical measurements providing the fraction of empty space in the opal volume. Optical measurements yielded the position of the maximum of the reflectance band produced by diffraction from the (111) planes of the fcc lattice of an unloaded opal. As follows from the Bragg law, $\lambda = 2n_{eff}d$ in the case of normal incidence of light on the sample surface. The effective refractive index has been found as $n_{eff}^2 = n_{\text{SiO}_2}^2 f_{\text{SiO}_2} + n_{\text{TiO}_2}^2 f_{\text{TiO}_2} + f_{\text{air}}$, where n_{SiO_2} , n_{TiO_2} , and f_{SiO_2} , f_{TiO_2} are the refractive indices and volume fractions of silica and anatase, respectively. The replacement of air in the opal voids by optical oil with a known refractive index produces a red shift of the diffraction maximum. Knowing the refractive indices of silica and anatase (1.43 and 2.3, respectively) and assuming that the lattice constant remains unchanged and that the volume fraction of silica is equal to 0.74, one

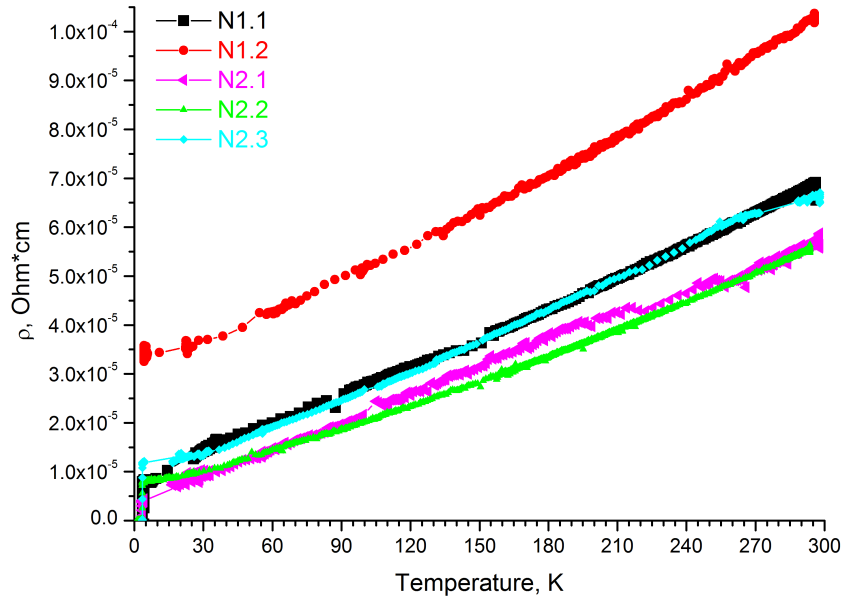


Figure 4.3: Temperature dependences of resistivity of In-opal samples 1.1, 1.2, 2.1, 2.2, and 2.3.

can readily solve the two equations for the volume fraction of anatase and air in the opal matrix.

Next, the TiO_2 layer thickness was derived from the expression

$$\delta = cD \left(1 - \frac{f_{\text{overgrown}}}{f_{\text{origin}}} \right), \quad (4.3)$$

where $f_{\text{overgrown}}$ is the free volume fraction of the overgrown opal, f_{origin} is the free volume fraction of the original opal without the oxide layers, and $c = 1/(\pi\sqrt{2}) - 1/6 \approx 0.0584$. Equation (4.3) is valid in the case of spheres contacting at one point and can be derived from the relation

$$\frac{f_{\text{overgrown}}}{f_{\text{origin}}} = \frac{V_{\text{origin}} - S_{\text{inner}}\delta}{V_{\text{origin}}}, \quad (4.4)$$

where V_{origin} is the volume of the original opal and S_{inner} is the total inner opal surface area. The total layer thicknesses δ calculated by the above methods varies by less than $\Delta\delta = 2$ nm for all samples except for sample 1.3. In sample 1.3 the variation is about 4 nm. Such difference is attributed to the fact that the void size has been modified by combination of the both methods, SiO_2 deposition and subsequent TiO_2 layer-by-layer overgrowth.

As for the indium-porous glass (In-PG) samples, the porous matrix has been prepared from sodium

borosilicate glass. The average pore size determined by the mercury-intrusion porosimetry method is 70 Å in diameter. The pores in the glass are connected by narrow bridges. Therefore, nanoparticles of indium form a random interconnected network in a glass. During the manufacturing process the porous glass has been cleaned by hydrogen peroxide H_2O_2 . In order to remove the H_2O_2 from the pores, the glass has been heated to 130 °C in the air environment. The embedding process requires indium to be melted. Therefore, indium has been embedded into the porous glass under high pressure up to 9 Kbar at 165 °C. Electrical resistance has been measured by standard a four-probe method.

4.2 Superconducting transitions

All the presented samples of the indium–opal nanocomposite reveal a superconducting transition. It is evident from Figs. 4.4, 4.5, 4.6 and Table 4.1 that the critical temperatures and critical magnetic fields of the superconducting transition noticeably exceed those of the bulk indium. The corresponding critical values of bulk indium are $T_c^{bulk} = 3.41$ K and $H_c^{bulk}(0) = 280$ Oe. As can be seen from Fig. 4.7, magnetic field destroys superconductivity and restores the sample resistivity to its normal-state value, $\rho = \rho_N$. Data in Table 4.1 shows a correlation of critical parameters T_c and H_c2 with the indium grain size within the same group of samples. The correlation is inverse. The samples with larger number of TiO_2 layers exhibit higher T_c and H_c2 . Meaning that the smaller the size of the indium particles the higher the degeneracy of indium grains in comparison with the bulk indium which results in higher values of transition temperature and critical magnetic field. At the same time, the reduction of the indium grain size is accompanied by an increase in the electrical resistivity of a sample $\rho_s = (S_s/l_s)R$ in the normal state directly before the SC transition. Also the slope of the resistivity temperature dependence $R(T)$ becomes smoother, as depicted in Figs. 4.2 and 4.3. The resistivity measurements show metallic behavior, see Figs. 4.2 and 4.3. However, $\rho_s(T)$ dependence of the sample with the most narrow bridges $d_b \approx 10$ nm exhibit a nonmetallic character: $\rho_s(300K)/\rho_s(4.2K) \approx 0.7$, see Figs. 4.2 and 4.3.

The most intriguing feature of Figs. 4.4 and 4.5 is enhancement of critical temperatures with increasing disorder and resistivity. The samples 1.3 and 2.4 show wide superconducting transition wherein the onset temperature of superconductivity is anomalously large. This is in contrast with usual behavior. Indeed, experimentally it is well established that the critical temperature decreases monotonically as disorder increases (Tashiro et al. (2008)). Theoretical studies has shown that this reduction of the critical temperature can be explained by the interplay between weak disorder and Coulomb interactions (Maekawa et al. (1984)). For stronger disorder near the superconductor-insulator transition it has been shown numerically (Bouadim et al. (2011)) that, even in the absence of Coulomb interactions, phase fluctuations are enhanced (Mondal et al. (2011)) and the superconducting order parameter becomes highly inhomogeneous (Sherman et al. (2014)). This is consistent with experimental observations of a universal scaling of the order parameter amplitude distribution

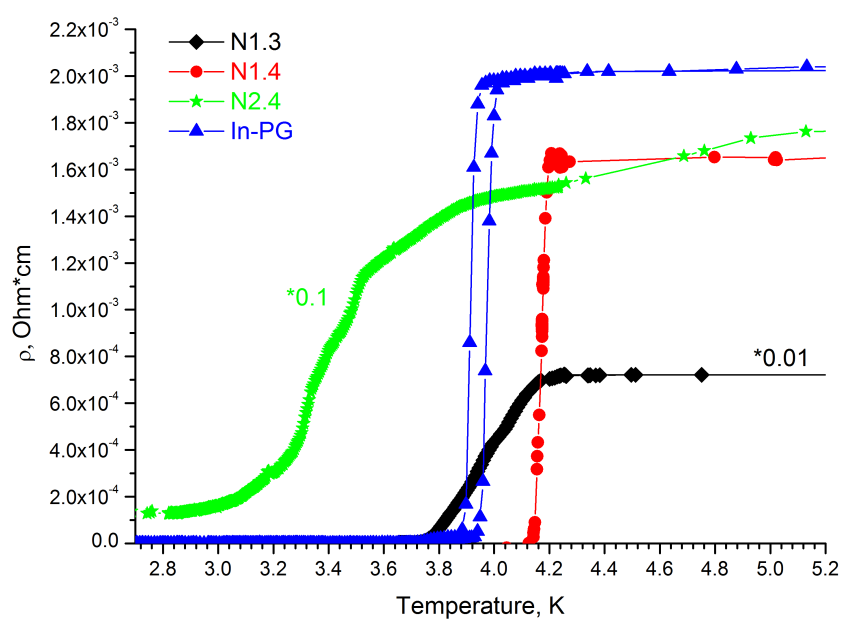


Figure 4.4: Superconducting transition in In-opal nanocomposite samples 1.3, 1.4, 2.4, and In-porous glass.

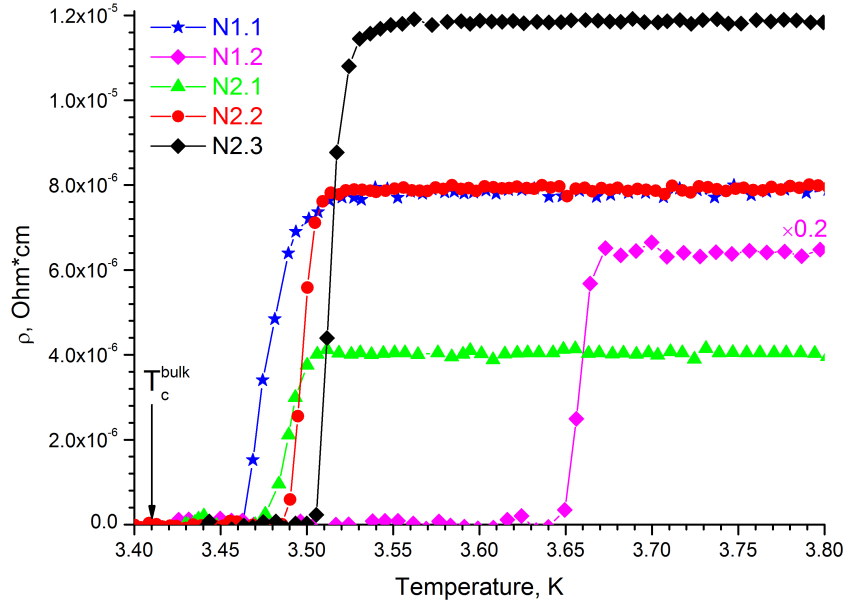


Figure 4.5: Superconducting transition in In-opal nanocomposite samples 1.1, 1.2, 2.1, 2.2, and 2.3.

function (Lemarie et al. (2013)), emergent granularity (Brun et al. (2014)) and reports of glassy features (Ioffe and Mezard (2010)), with a supercurrent flow pattern reminiscent of a percolative cluster (Seibold et al. (2012)), a pseudo-gap phase (Bouadim et al. (2011)) and preformed Cooper pairs (Sacepe et al. (2011)) for sufficiently strong disorder (Mayoh and Garcia-Garcia (2014c)).

Strong disorder produces inhomogeneity in the order parameter with strong phase fluctuations. As a result the superconductivity is suppressed in comparison to the clean limit. The Anderson theorem does not really apply in this region as self-averaging, one of its assumptions, is not expected to hold for sufficiently strong disorder (Suslov (2013)). However, recent theoretical studies have suggested that enhancement might indeed occur in the presence of strong disorder. The density matrix renormalization group analysis of Ref. (Tezuka and Garcia-Garcia (2010)) showed that phase coherence in a one dimensional disordered Hubbard model with attractive interactions at zero temperature is enhanced for weak coupling and disorder close to but below the superconductor-insulator threshold. In Refs. (Feigel'man et al. (2007)) it was reported that superconductivity was strongly enhanced around the Anderson metal-insulator transition. The origin of this enhancement is directly related to the multifractality of eigenstates of the one-body problem in the critical regime (Falkó and Efetov (1995)). The strong spatial correlations of multifractal eigenstates (Fyodorov and Mirlin (1997)) around the Fermi energy lead to a more robust superconducting state (Mayoh and Garcia-Garcia

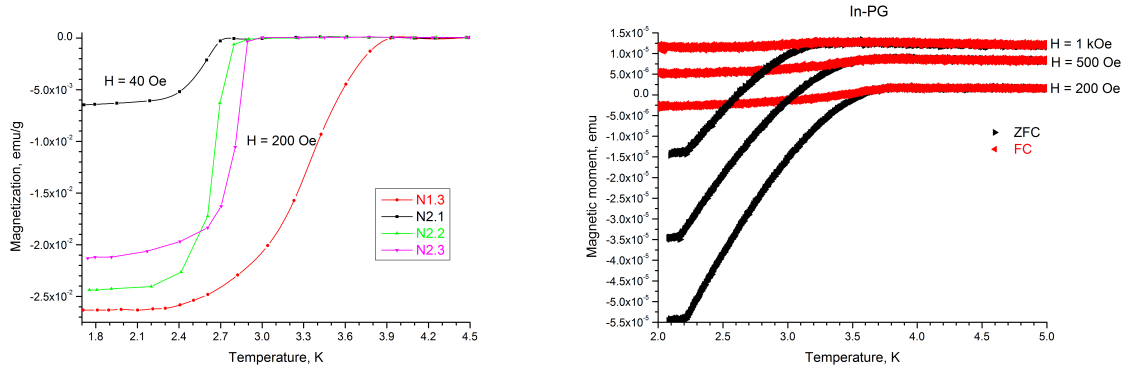


Figure 4.6: Temperature dependence of magnetization of In-opal and magnetic moment of In-porous glass at superconducting transition. (Left) In-opal samples 1.3, 2.2, 2.3 in magnetic field $H = 200$ Oe, and 2.1 in field $H = 40$ Oe. (Right) In-porous glass sample in magnetic fields $H = 200, 500, 1000$ Oe.

(2014c)). The problem for disordered systems around an Anderson transition characterized by multifractal one-body eigenstates has been addressed in Ref. (Mayoh and Garcia-Garcia (2014c)). In the limit of weak multifractality and for weakly coupled superconductors the superconducting order parameter has been computed analytically, including its energy dependence and statistical distribution in space. Computations using percolation techniques in the absence of phase fluctuations show that the critical temperature is greater than that of the clean limit only for very weakly coupled superconductors. Such predictions have been experimentally observed only in aluminum thin films which is a very weakly coupled metallic superconductor. Consistent with the computations no enhancements have been discovered in strongly coupled materials.

From the theoretical point of view the problem of global superconductivity in disordered superconductors is still under debate. This is emphasized by the title of the Ref. (Mayoh and Garcia-Garcia (2014c)) "Can disorder really enhance superconductivity?". There are some arguments about possibility for large increase of critical temperature by disorder (Suslov (2013, 2015)) and scepticism about that (Mayoh and Garcia-Garcia (2014c)).

The MG model described in Chapter 3 (Mayoh and Garcia-Garcia (2014b)) gives reasonable explanation to experimental results. As can be seen from Figs. 4.4-4.6 two groups of samples can be discerned. In first group, superconducting transition is narrow, i. e. $T_c^{\text{Array}} \approx T_c^{\text{on}}$ and increases monotonously with decreasing of the granular size and growing of the resistance. The highest $T_c^{\text{Array}} = 4.15$ K is found which considerably exceeds bulk $T_{c0} = 3.41$ K. In second group, the transition is wide T_c^{Array} is significantly less than T_c^{on} . In these samples the resistivity has been found to be approximately two orders of magnitude higher than that of the other In-opal samples. T_c^{on} can reach 5 K. In disordered In-porous glass samples relatively wide superconducting transition is

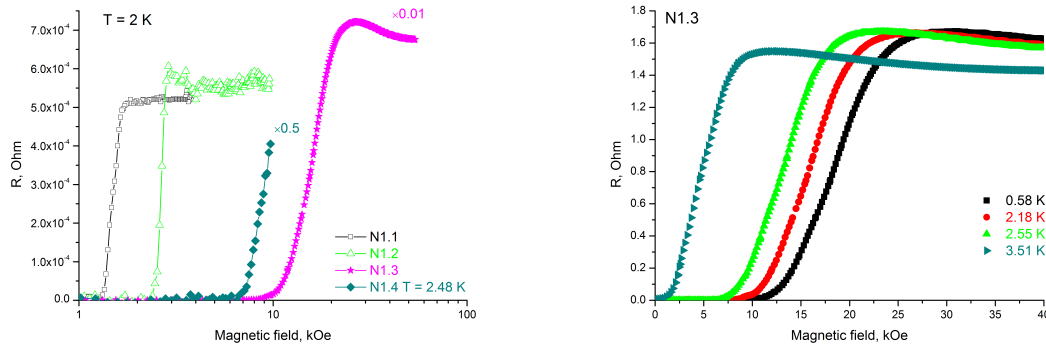


Figure 4.7: (Left) Magnetic field dependences of resistivity of In-opal samples 1.1, 1.2, 1.3 at 2 K and sample 1.4 at 2.48 K. (Right) Temperature evolution of magnetic field dependences of resistivity of In-opal sample 1.3.

observed. In this case $T_c^{\text{on}} = 3.95 - 3.97$ and $T_c^{\text{Array}} = 3.7 - 3.9$ are found which are consistent with results obtained previously by other authors. The resistivity values of In-porous glass samples are between those of the first and the second groups of In-opals. The obtained results can be qualitatively explained by mentioned above theory, where two regimes of phase transition have been predicted depending on resistivity. The transition that breaks global-phase coherence goes from being percolation at low resistivity to phase-fluctuation driven at high resistivity. This corresponds to the crossover from first to second group in ordered In-opal system assuming existence of a maximum for T_c^{Array} between them. Disordered systems have not been considered in that theory but one can suggest that in indium-porous glass the phase-fluctuations are important. Because of the similarity of the results for In-porous glass obtained by different groups T_c^{Array} is weakly dependent on resistivity in this case and considerably less than maximum value for In-opals. In MG theory all resistivity is connected with intergranular tunneling, i. e. the increasing of resistivity means their disordering. For In-opal systems this corresponds to the second group of studied samples. But for the first group it is only an approximation. One can suggest that this approximation is quite good for the maximum of T_c^{Array} .

Figure 4.7 shows the magnetic field dependences of resistivity of In-opal samples 1.1, 1.2, 1.3 at 2 K and sample 1.4 at 2.48 K (left panel) and of In-opal sample 1.3 at different temperatures (right panel). The superconducting transition widths in temperature, ΔT_c , and in magnetic field, ΔH_c , have been determined from the resistivity decline as the difference in temperature (or magnetic field) between the $0.9\rho_N$ and $0.1\rho_N$ levels. Whereas, the critical temperature T_c and upper critical field H_{c2} have been derived at the $\rho = 0.5\rho_N$ level. Samples with a comparatively high volume fraction of indium ($f_{\text{In}} = 0.17-0.26$) display a narrow superconducting transition, $\Delta T_c < 0.1$ K and $\Delta H_c < 100$ Oe (Fig. 4.7). While the superconducting transition in samples 1.3 and 2.4 characterized

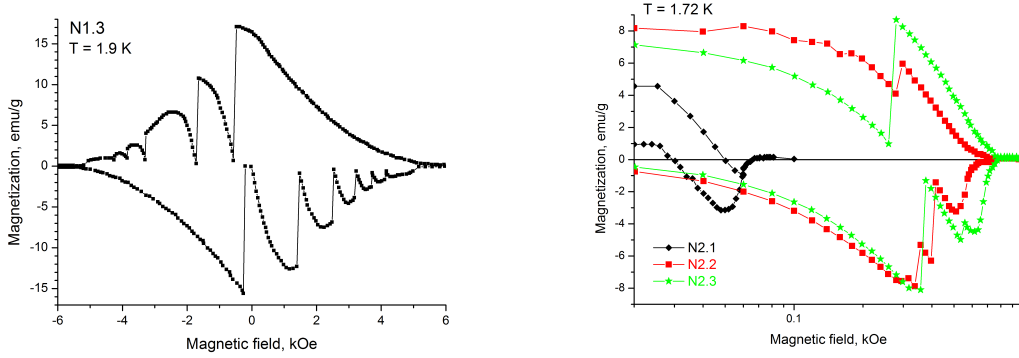


Figure 4.8: (Left) Magnetic field dependences of magnetization of In-opal sample number 1.3 at 1.9 K. (Right) Magnetic field dependences of magnetization of In-opal samples 2.1, 2.2, 2.3 at 1.72 K.

by a relatively small volume fraction of the conducting part $f_{In} < 17\%$ is broad both in temperature and in magnetic field. Therefore, Table 4.1 presents two values of T_c and $H_c(0)$ for these samples. The values listed in Table 4.1 are the boundaries of the interval within which the parameters vary between the $0.9\rho_N$ and $0.1\rho_N$ levels. Sample 1.4 occupies an intermediate position. One can observe a sharp superconducting transition which splits into two transitions with critical temperatures that are close in magnitude. Also, the critical magnetic field in sample 1.3 extrapolated to $T = 0$ exceeds $H_c^{bulk}(0)$ by about 70 times (D. V. Shamshur and Romanov (2000)).

4.3 Thermomagnetic instabilities in magnetization

Magnetic instabilities in type-II superconductors have been known for more than 40 years (Mints and Rakhmanov (1981); Altshuler and Johansen (2004)). It is generally assumed that the occurrence of magnetic instabilities is caused by abrupt redistribution of Abrikosov vortices triggered by temperature fluctuations. This physical phenomenon is also called thermomagnetic instabilities. Magnetic field higher than H_{c1} starts to penetrate into a type-II superconductor in a form of Abrikosov vortices. The vortices hold magnetic flux quanta enclosed by circulating superconducting currents J_c . Defects in a material produce pinning center which capture Abrikosov vortices, resulting in inhomogeneous flux distribution over the sample volume. Hence, there is a spatial variation of magnetic field with critical supercurrents J_c flowing around vortices in the sample. The system relaxes to equilibrium which is called critical state. If a small perturbation occurs, such as local temperature fluctuation, vortices start to move in order to adjust a new critical current corresponding to the altered temperature. The energy dissipation produced by moving flux lines leads to a local increase in temperature. If the latter is smaller than the initial fluctuation, the critical state remains stable. Otherwise, the temperature increase results in new adjustment of the critical current,

then again and again. This leads to vortex avalanches and pronounced flux jumps.

The most studied bulk superconductors with thermomagnetic instabilities are the conventional low-temperature superconductor Nb and its alloys (Mints and Rakhmanov (1981); Kim et al. (1963)), as well as YBaCuO and some others high- T_c superconductors (Muller and Andrikidis (1994); Gerber et al. (1993)), and MgB₂ (Romero-Salazar et al. (2007); Chabanenko et al. (2003)), which have low heat capacity and possibility to transport high enough J_c . For YBaCuO (Muller and Andrikidis (1994)), Nb-plate (Chabanenko et al. (2000)) and MgB (Chabanenko et al. (2003); Romero-Salazar et al. (2007)) numerical calculations showed the validity of the adiabatic limit for treating the magnetization jumps within a large range of the field sweep rate. More general numerical approach which involves the kinetics of heat exchange with the environment was suggested in Ref. (Zhou and Yang (2006)). The magnetization jumps in superconducting thin films have been observed to have forms different from the homogeneous Bean magnetic profiles, for instance, dendrite and branched fingerlike patterns as well as feather-shaped flux fronts (Altshuler and Johansen (2004); Prozorov et al. (2006); Yurchenko et al. (2007)). The later was referred to the enhanced pinning in thin superconducting films (Silhanek et al. (2004)). As for the superconducting nanocomposites, such magnetic instabilities have been revealed only in a Vycor glass with indium inclusions (Watson (1970)). The butterfly-like hysteresis (also called fishtail) has been found in many high- T_c superconductors (Kodama et al. (1997); Yang et al. (1997); Wang et al. (1997)). This effect can be treated in different ways. Particularly, a Josephson junction model of fishtail was discussed in Ref. (Osofsky et al. (1992)). This model agrees well with the model of strongly and weakly coupled metallic crystallites in porous matrices.

Zero-field cooled (ZFC) and field-cooled (FC) magnetizations presented in Fig. 4.6 reveal behavior typical for type-II superconductors with the critical temperature close to that in bulk indium. The magnetization versus magnetic field hysteresis loops reveal magnetic instabilities. Figure 4.8 shows magnetic field dependences of magnetization of In-opal sample 1.3 at 1.9 K (left panel) and samples 2.1, 2.2, 2.3 at 1.72 K (right panel). Sharp phase transitions in the mixed state are clearly visible from these plots manifesting themselves as magnetization jumps. Similar peculiarities in magnetization curves were observed in Pb-opal nanocomposites (Aliev et al. (2007)). In the mixed state at relatively low temperatures, $T < 5.5$ K the Pb inverse opal revealed a series of magnetization jumps showing the magnetization response of transitions in the fluxoid states. This was achievable only for red opal with a particle size comparable to or bigger than the coherence length, $r \geq \xi$. The number of fluxoid transitions increases at lower temperatures (ξ is decreased). The transition between fluxoid states is reversible without measurable hysteresis. The results for sample 1.3 are of special interest because of they demonstrate both the strong pinning due to high resistivity and preserved effects of structural ordering which are characterised by sharp jumps to zero value of magnetization. Such behavior proves the correlating nature of the disorder and pinning. It should be noted here that in normal state this sample shows non-metallic behavior with preformed Cooper pairs near boson

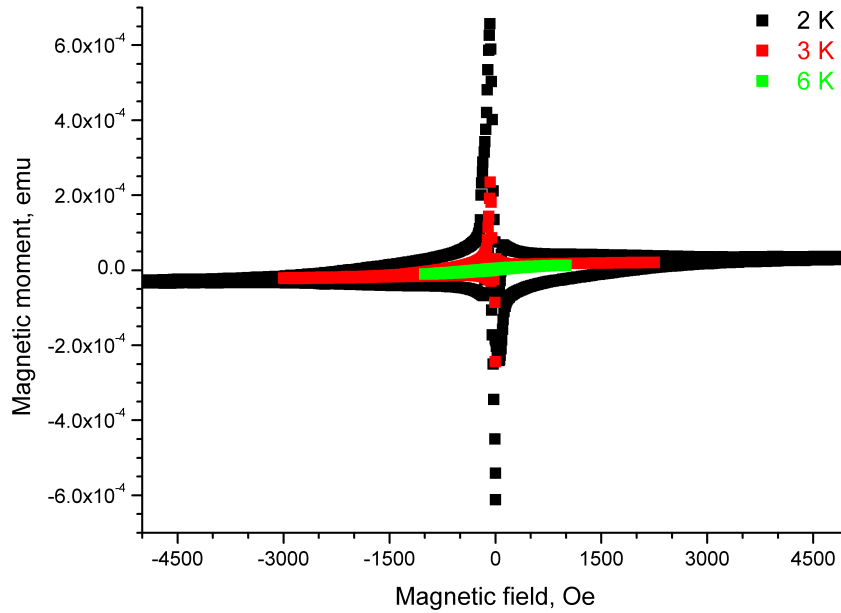


Figure 4.9: Magnetic field dependences of magnetization of In-PG at $T = 2, 3$, and 6 K.

localization transition. Also similar magnetization jumps were observed in numerical simulation of Josephson junctions in the external magnetic field (Luca et al. (1998)). Figure 4.9 shows magnetic field dependences of magnetization of In-PG sample at temperatures $T = 2, 3$, and 6 K. Because of small size of granules and their irregular positions the Josephson effect is averaged and the effective critical state Bean model can be applied. The form of the obtained curves is similar that of Ga-porous glass data (Charnaya et al. (1998)).

The flux jumps in type-II superconductors are often experimentally observed by measuring the magnetization at sweeping external magnetic field H_e (Hebert et al. (2003); Gerber et al. (1993); Romero-Salazar et al. (2007)). The flux jumps manifest themselves on hysteresis loops $M(H_e)$ as abrupt reduction in magnetization followed by gradual recovering. The change in external magnetic field H_e leads to an increase of the local temperature in the material. Depending on the final temperature established as a result of a flux jump, the corresponding magnetization jumps can be small or giant, as is observed in Figs. 4.8 and 4.9. Various physical parameters influence the occurrence and form of the jumps such as the temperature, critical current, thermal conductivity, specific heat, demagnetization factor, etc. Hence, the variety of the parameters complicates the understanding of the role of each of them in magnetization jumps. Two main approximations have been suggested to establish the behavior of the vortices to the local overheating (Kim et al. (1963); Hancox (1965)). The dynamic approximation corresponds to the case when the diffusivity of magnetic flux is smaller

than the thermal diffusion coefficient leading to spreading heat through frozen vortex and current system. The opposite case is that of adiabatic heating when the thermal diffusivity is smaller than the magnetic one.

As can be seen from Figs. 4.8 and 4.9, the magnetic properties of the samples in the superconducting state are rather different. Nevertheless, diamagnetic shielding is strong enough at low temperatures for all specimens. The superconducting screening currents circulate over indium nanoparticles in at least several neighboring pores and that the external magnetic field is pushed out from the most volume of the samples makes it possible to analyze the system with a model of porous glasses filled with metals developed in Refs. (Charnaya et al. (1995, 1996)).

Thus, following the treatment in Ref. (Charnaya et al. (1996)) the indium in porous glass can be modeled as a disordered three-dimensional network of grains formed by strongly coupled metallic crystallites, where the grains are connected by weak Josephson links. The superconducting properties of the grains are described by the theory of type-II superconductors. It is known that three-dimensional arrays of Josephson junctions can undergo a well resolved double superconducting phase transition depending on intergranular resistance at temperatures when links responsible for intergranular phenomena are in the normal state (Deutscher et al. (1974); Ebner and Stroud (1983)). At high temperatures (close to the critical temperature) single grains become superconducting. As the temperature gets lower, the more grains undergo the superconducting transition and the total number of the superconducting grains in the system increases. At some point the order parameter of the individual grains become coherent. The suppression of the phase ordering transition temperature T_j is regulated by the following relation (Ebner and Stroud (1983); Jardim et al. (1994)):

$$\frac{T_j}{T_c} = \frac{1}{1 + \beta R/R_0}, \quad (4.5)$$

where T_c is the temperature of the superconducting transition in grains, β is the numerical coefficient of the order of 0.1, R is the normal-state intergrain resistance, and $R_0 = \hbar/e^2$ is a characteristic resistance. The relationship Eq. (4.5) has been obtained with the following assumptions, superconducting grains are equal in size and the distribution of barrier resistance is neglected. Percolative disordering also leads to reducing the temperature of the transition to global superconductivity (Ebner and Stroud (1983); Harris et al. (1991)). Therefore, the percolative disorder and increase of tunneling resistivity widen the temperature range of the superconducting transition. The double resistive transitions were observed experimentally for some electron-doped granular superconductors (Jardim et al. (1994); Diaz et al. (1997); Jardim et al. (1997a)). It then follows from Eq. (4.5) that when $R \ll R_0$ the shift of T_j is negligibly small and the superconducting phase transition is sharp. This is the case of the indium-porous glass system and indium-opal samples N1.5, N2.2, N2.3, and N3.4. A roughly linear temperature dependence of the upper critical field agrees with such a conclusion (see Table 4.1). The broad superconducting transitions in other samples can be attributed to

smaller sizes of effective grains (Halperin (1986)). In fact, the greater distance between pores leads to a weakening of the coupling between indium nanoparticles. Indium confined in ordered silica spheres can be viewed as indium grains interconnected with narrow bridges. These bridges serve as weak Josephson links with high resistance in normal state. The reversible behavior of magnetization (Figs. 4.9) within a temperature range where most of intergranular links are still in normal state then signifies that the number of pins within the grains is very small. This agrees with regular local packing of silica spheres in opals seen by electron microscopy, see Fig. 4.1.

Recently, strong enhancement of superconducting critical temperature, T_c^{Array} , in nanogranular composites by shell effects has been predicted (Mayoh and Garcia-Garcia (2014b)). The highest T_c^{Array} has been found for intermediate resistances and for face-centered cubic array. The present work describes and discusses the enhancement of superconductivity in indium-opal and indium-porous glass nanocomposites in comparison to the bulk indium from the point of view of finite size effects. It is suggested that shell and inhomogeneous pairing effects as well as phase fluctuations can drastically influence superconducting critical temperature in both ways, increasing or decreasing it. The superconductivity is analyzed based on transport and magnetization measurements of In-opal and In-porous glass nanocomposites. Opals with different nanosizes are investigated. The size lowering leads to an increase of resistivity of the samples. The indium-opal samples are split into two categories upon the present disorder in them. The disorder is evaluated by the number of TiO_2 layers deposited inside the opal spheres prior to the indium injection. As well as by resistance.

In disordered indium-porous glass samples relatively wide superconducting transition is observed, in particular $T_c^{\text{on}} = 3.95 - 3.97$ and $T_c^{\text{Array}} = 3.7 - 3.9$. The resistivity values of In-porous glass samples are between those of the first and the second groups of In-opals. The obtained results can be qualitatively explained by mentioned above theory, where two regimes of phase transition have been predicted depending on resistivity. The transition that breaks global-phase coherence goes from being percolation at low resistivity to phase-fluctuation driven at high resistivity. This corresponds to the crossover from first to second group in ordered In-opal system assuming existence of a maximum for T_c^{Array} between them. For In-porous glass T_c^{Array} weakly correlates with resistivity and is considerably less than the maximum value of the critical temperature for In-opals. In Mayoh-Garcia theory all resistivity is connected with intergranular tunneling, i. e. the increasing of resistivity means their disordering. For In-opal systems this corresponds to the second group of studied samples. But for the first group it is only an approximation. One can suggest that this approximation is quite good for the maximum of T_c^{Array} .

Taking into account that theoretically predicted $T_c^{\text{Array}}/T_{c0} = 3.5$ can be achieved, investigation of superconducting nanocomposites based on opal and porous glass systems can serve as a platform for studying of shell superconducting effects in engineered nanocomposites.

- Abeles, B., Cohen, R. W., Cullen, G. W., 1966. Phys. Rev. Lett. 17, 632.
- Aliev, A. E., Lee, S. B., Zakhidov, A. A., Baughman, R. H., 2007. Physica C 453, 15.
- Altshuler, E., Johansen, T. H., 2004. Rev. Mod. Phys. 76, 471.
- Anderson, P. W., 1959. J. of Phys. and Chem. of Solids 11, 26.
- Anderson, P. W., Muttalib, K. A., Ramakrishnan, T. V., 1983. Phys. Rev. B 28, 117.
- Balakirev, V. G., Bogomolov, V. N., Zhuravlev, V. V., Kumrezov, Y. A., Petranovskii, V. P., Romanov, S. G., Samoilovich, L. A., 1993. Crystallogr. Rep. 38, 348.
- Ballesteros, H. G., Fernandez, L. A., Martin-Mayor, V., Sudupe, A. M., Parisi, G., Ruiz-Lorenzo, J. J., 1999. J. Phys. A: Math. Gen. 32, 1.
- Bardeen, J., Cooper, L., Schrieffer, J., 1957. Phys. Rev. 108, 1175.
- Bennemann, K. H., Ketterson, J. B., 2008. Superconductivity: Conventional and Unconventional Superconductors Volume 1, Springer.
- Bezryadin, A., Lau, C. N., Tinkham, M., 2000. Nature 404, 971.
- Blatt, J. M., Thompson, C. J., 1963. Phys. Rev. Lett. 10, 332.
- Bogomolov, V., Kumzerov, Y., Romanov, S., Zhuravlev, V., 1993. Physica C 208, 371.
- Bogomolov, V. N., Kazantseva, L. K., Kolla, E. V., Kumzerov, Y. A., 1987. Sov. Phys. Solid State 29, 359.
- Bogomolov, V. N., Zhuravlev, V. V., and E. V. Kolla, A. I. Z., Kumzerov, Y. A., 1982. JETP Lett. 36, 365.
- Bose, S., Bhattacharya, V., Chattopadhyay, K., Ayyub, P., 2005a. Phil. Mag. Lett. 85, 577.
- Bose, S., Bhattacharya, V., Chattopadhyay, K., Ayyub, P., 2008. Acta Mater. 56, 4522.

- Bose, S., Galande, C., Chockalingam, S. P., Banerjee, R., Raychaudhuri, P., Ayyub, P., 2009. J. Phys.: Condens. Matter 21, 205702.
- Bose, S., Garcia-Garcia, A. M., Ugeda, M. M., Urbina, J. D., Michaelis, C. H., Brihuega, I., Kern, K., 2010. Nature Materials 9, 550.
- Bose, S., Raychaudhuri, P., Banerjee, R., Ayyub, P., 2006. Phys. Rev. B 74, 224502.
- Bose, S., Raychaudhuri, P., Banerjee, R., Vasa, P., Ayyub, P., 2005b. Phys. Rev. Lett. 95, 147003.
- Bouadim, K., Loh, Y. L., Randeria, M., Trivedi, N., 2011. Nat. Phys. 7, 884.
- Boyaci, H., Gedik, Z., Kulik, I., 2001. J. of Supercond. 14, 133.
- Brack, M., Bhaduri, R., 1997. Semiclassical Physics, Addison–Wesley, New York.
- Brihuega, I., Garcia-Garcia, A. M., Ribeiro, P., Ugeda, M. M., Michaelis, C. H., Bose, S., Kern, K., 2011. Phys. Rev. B 84, 104525.
- Brun, C., Cren, T., Cherkez, V., Debontridder, F., Pons, S., Fokin, D., Tringides, M., Bozhko, S., Ioffe, L., Altshuler, B., 2014. Nat. Phys. 10, 444.
- Chabanenko, V., Puzniak, R., Nabialek, A., Vasiliev, S., Rusakov, V., Huanqian, L., Szymczak, R., Szymczak, H., Jun, J., Karpinski, J., Finkel, V., 2003. J. Low Temp. Phys. 130, 175.
- Chabanenko, V. V., D'yachenko, A. I., Zalutskii, M. V., Rusakov, V. F., Szymczak, H., Piechota, S., Nabialek, A., 2000. J. Appl. Phys. 88, 5875.
- Chakravarty, S., Kivelson, S., Zimanyi, G. T., Halperin, B. I., 1987. Phys. Rev. B 35, 7256.
- Charnaya, E. V., Kumzerov, Y. A., Tien, C., Wur, C. S., 1995. Solid State Commun. 94, 635.
- Charnaya, E. V., Tien, C., Lee, M. K., Kumzerov, Y. A., 2009. J. Phys.: Condens. Matter 21, 455304.
- Charnaya, E. V., Tien, C., Lin, K. J., Wur, C. S., Kumzerov, Y. A., 1998. Phys. Rev. B 58, 467.
- Charnaya, E. V., Tien, C., Wur, C. S., Kumzerov, Y. A., 1996. Physica C 269, 313.
- Ciou, Y. S., Lee, M. K., Charnaya, E. V., Tien, C., Chang, L. J., Kumzerov, Y. A., Samoylovich, M. I., 2013. Supercond. Sci. Technol. 26, 055009.
- Ciou, Y. S., Tien, C., Charnaya, E. V., Xing, D. Y., Lee, M. K., Kumzerov, Y. A., Pirozerskii, A. L., 2012. Physica C 477, 51.
- Crane, R., Armitage, N. P., Johansson, A., Sambandamurthy, G., Shahar, D., Grüner, G., 2007. Phys. Rev. B 75, 184530.

- Croitoru, M. D., Shanenko, A. A., Kaun, C. C., Peeters, F. M., 2011. Phys. Rev. B 83, 214509.
- D. V. Shamshur, A. V. Chernyaev, A. V. F., Romanov, S. G., 2000. Nanostructures: Phys. and Tech. 38, (Ioffe Institute, St. Petersburg, p. 311).
- de Gennes, P., 1964. Rev. Mod. Phys. 36, 225.
- Delft, J. V., 2001. Annalen der Physik 10, 219.
- Delft, V. J., Zaikin, A., Golubev, A. S., Tichy, W., 1996. Phys. Rev. Lett. 77, 3189.
- Deutscher, G., Fenichel, H., Gershenson, M., Grünbaum, E., Ovadyahu, Z., 1973. J. Low Temp. Phys. 10, 231.
- Deutscher, G., Imry, Y., Gunther, L., 1974. Phys. Rev. B 10, 4598.
- Diaz, A., Maza, J., Vidal, F., 1997. Phys. Rev. B 55, 1209.
- Dong, F., Graf, M. J., Huber, T. E., Huber, C. I., 1997. Solid State Commun. 101, 929.
- Driessen, E. F. C., Coumou, P. C. J. J., Tromp, R. R., de Visser, P. J., Klapwijk, T. M., 2012. Phys. Rev. Lett. 109, 107003.
- Dubi, Y., Meir, Y., Avishai, Y., 2007. Nature 449, 876.
- Dynes, R. C., Garno, J. P., Hertel, G. B., Orlando, T. P., 1984. Phys. Rev. Lett. 53, 2437.
- Dynes, R. C., Narayanamurti, V., Garno, J. P., 1978. Phys. Rev. Lett. 41, 1509.
- Ebner, C., Stroud, D., 1983. Phys. Rev. B 28, 5053.
- Eley, S., Gopalakrishnan, S., Goldbart, P. M., Mason, N., 2012. Nat. Phys. 8, 59.
- Emery, V. J., Kivelson, S. A., 1995. Nature 374, 434.
- Falkó, V. I., Efetov, K. B., 1995. Europhys. Lett. 32, 627.
- Farine, M., Hekking, F. W. J., Schuck, P., Vinas, X., 2001. Phys. Rev. B 63, 125319.
- Feigel'man, M., Ioffe, L. B., Kravtsov, V. E., Yuzbashyan, E. A., 2007. Phys. Rev. Lett. 98, 027001.
- Feigel'man, M., Skvortsov, M. A., 2012. Phys. Rev. Lett. 109, 147002.
- Finkelstein, A. M., 1987. JETP Lett. 45, 46.
- Fisher, M. P. A., 1990. Phys. Rev. Lett. 65, 923.
- Fyodorov, Y. V., Mirlin, A. D., 1997. Phys. Rev. B 55, R16001.

- Gantmakher, V. F., Dolgoplov, V. T., 2010. Phys. Usp. 53, 1.
- Garcia-Garcia, A., Urbina, Y., Yuzbashyan, E., Richter, K., Altshuler, B., 2011. Phys. Rev. B 83, 014510.
- Gerber, A., Li, J. N., Tarnawski, Z., Franse, J. J. M., Menovsky, A. A., 1993. Phys. Rev. B 47, 6047.
- Ghosal, A., Randeria, M., Trivedi, N., 1998. Phys. Rev. Lett. 81, 3940.
- Ghosh, S., Mandal, S. S., 2013. Phys. Rev. Lett. 111, 207004.
- Giaever, I., Zeller, H. R., 1968. Phys. Rev. Lett. 20, 1504.
- Gladilin, V. N., Fomin, V. M., Devreese, J. T., 2002. Solid State Comm. 121, 519.
- Gladilin, V. N., Tempere, J., Silvera, I. F., Devreese, J. T., 2006. Phys. Rev. B 74, 104512.
- Goldman, A. M., Markovic, N., 1998. Phys. Today 51, 39.
- Graf, M. J., Huber, T. E., Huber, C. A., 1992. Phys. Rev. B 45, 3133.
- Guo, Y., Zhang¹, Y.-F., Bao, X.-Y., Han, T.-Z., Tang, Z., Zhang, L.-X., Zhu, W.-G., Wang, E. G., Niu, Q., Qiu, Z. Q., Jia, J.-F., Zhao, Z.-X., Xue, Q.-K., 2004. Science 306, 1915.
- Halperin, W. P., 1986. Rev. Mod. Phys. 58, 533.
- Hancox, R., 1965. Phys. Lett. 16, 208.
- Harris, D. C., Herbert, S. T., Stroud, D., Garland, J. C., 1991. Phys. Rev. Lett. 67, 3606.
- Haviland, D. B., Liu, Y., Goldman, A. M., 1989. Phys. Rev. Lett. 62, 2180.
- Hebert, S., Look, L. V., Weckhuysen, L., Moshchalkov, V. V., 2003. Phys. Rev. B 67, 224510.
- Heiselberg, H., 2003. Phys. Rev. A 68, 053616.
- Ioffe, L. B., Mezard, M., 2010. Phys. Rev. Lett. 105, 37001.
- Jardim, R. F., Ben-Dor, L., Stroud, D., Maple, M. B., 1994. Phys. Rev. B 50, 10080.
- Jardim, R. F., Westphal, C. H., Becerra, C. C., Paduan, A., 1997a. Phys. Rev. B 55, 1209.
- Jardim, R. F., Westphal, C. H., Becerra, C. C., Paduan, A., 1997b. J. Appl. Phys. 81, 4250.
- Jin, G., Zhang, J., Cai, C., Yao, X., Cao, S., 2008. J. Supercond. Nov. Magn. 21, 107.
- Kim, Y. B., Hempstead, C. F., Strand, A. R., 1963. Phys. Rev. 129, 528.

- Kim, Y. J., Overhauser, A., 1993. Phys. Rev. B 47, 8025.
- Kittel, C., 2004. Introduction to Solid State Physics 8th edition, Wiley.
- Kodama, Y., Oka, K., Yamaguchi, Y., Nishihara, Y., Kajimura, K., 1997. Phys. Rev. B 56, 6265.
- Kosterlitz, J. M., Thouless, D. J., 1973. J. Phys. C: Solid State Phys. 6, 1181.
- Kresin, V. Z., Ovchinnikov, Y. N., 2006. Phys. Rev. B 74, 024514.
- Lee, M. K., Charnaya, E. V., Tien, C., Chang, L. J., Kumzerov, Y. A., 2013. J. Appl. Phys. 113, 113903.
- Lee, M. K., Tien, C., Charnaya, E. V., Sheu, H.-S., Kumzerov, Y. A., 2010. Phys. Lett. A 374, 1570.
- Lemarie, G., Kamlapure, A., Bucheli, D., Benfatto, L., Lorenzana, J., Seibold, G., Ganguli, S. C., Raychaudhuri, P., Castellani, C., 2013. Phys. Rev. B 87, 184509.
- Liu, J., Wu, X., Ming, F., Wang, K., Xiao, X., 2013. Supercond. Sci. Technol. 26, 085009.
- Liu, J., Wu, X., Ming, F., Zhang, X., Wang, K., Wang, B., Xiao, X., 2011. J. Phys.: Condens. Matter 23, 265007.
- Luca, R. D., Matteo, T. D., Tuohimaa, A., Paasi, J., 1998. Phys. Rev. B 57, 1173.
- Maekawa, S., Ebisawa, H., Fukuyama, H., 1984. J. Phys. Soc. Japan 53, 2681.
- Mayoh, J., Garcia-Garcia, A. M., 2013. arXiv:1309.6255.
- Mayoh, J., Garcia-Garcia, A. M., 2014a. Phys. Rev. B 90, 014509.
- Mayoh, J., Garcia-Garcia, A. M., 2014b. Phys. Rev. B 90, 134513.
- Mayoh, J., Garcia-Garcia, A. M., 2014c. arXiv:1412.0029v2.
- Mayoh, J., Garcia-Garcia, A. M., 2015. arXiv:1502.06282.
- M.Garcia-Garcia, A., Urbina, J. D., Yuzbashyan, E. A., Richter, K., Altshuler, B. L., 2008. Phys. Rev. Lett. 100, 187001.
- Mints, R. G., Rakhmanov, A. L., 1981. Rev. Mod. Phys. 53, 551.
- Mondal, M., Kamlapure, A., Chand, M., Saraswat, G., Kumar, S., Jesudasan, J., Benfatto, L., Tripathi, V., Raychaudhuri, P., 2011. Phys. Rev. Lett. 106, 047001.
- Muller, K.-H., Andrikidis, C., 1994. Phys. Rev. B 49, 1294.

- Olofsson, H., Aberg, S., Leboeuf, P., 2008. Phys. Rev. Lett. 100, 037005.
- Osofsky, M. S., Cohn, J. L., Skelton, E. F., Miller, M. M., Soulen, R. J., Wolf, S. A., Vanderah, T. A., 1992. Phys. Rev. B 45, 4916.
- Panova, G. K., Naberezhnov, A. A., Fokin, A. V., 2008. Phys. Solid State 50, 1370.
- Panyukov, S. V., Zaikin, A. D., 1987. Phys. Lett. A 124, 325.
- Parmenter, R., 1968. Phys. Rev. 166, 392.
- Perali, A., Bianconi, A., Lanzara, A., Saini, N. L., 1996. Solid State Commun. 100, 181.
- Prozorov, R., Shantsev, D. V., Mints, R. G., 2006. Phys. Rev. B 74, 220511.
- Ralph, D. C., Black, C. T., Tinkham, M., 1995. Phys. Rev. Lett. 74, 3241.
- Rodriguez, A. H., Trallero-Giner, C., Ulloa, S. E., Marin-Antuna, J., 2001. Phys. Rev. B 63, 125319.
- Romanov, S. G., Fokin, A. V., Babamuratov, K. K., 1993. JETP Lett. 58, 824.
- Romero-Salazar, C., Morales, F., Escudero, R., Duran, A., Hernandez-Flores, O. A., 2007. Phys. Rev. B 76, 104521.
- Sacepe, B., Chapelier, C., Baturina, T. I., Vinokur, V. M., Baklanov, M. R., Sanquer, M., 2008. Phys. Rev. Lett. 101, 157006.
- Sacepe, B., Dubouchet, T., Chapelier, C., Sanquer, M., Ovadia, M., Shahar, D., Feigel'man, M., Ioffe, L., 2011. Nat. Phys. 7, 239.
- Schneider, R., Zaitsev, A. G., Fuchs, D., v. Löhneysen, H., 2012. Phys. Rev. Lett. 108, 257003.
- Seibold, G., Benfatto, L., Castellani, C., Lorenzana, J., 2012. Phys. Rev. Lett. 108, 207004.
- Shanenko, A. A., Croitoru, M. D., Peeters, F. M., 2006a. Europhys. Lett. 76, 498.
- Shanenko, A. A., Croitoru, M. D., Zgirski, M., Peeters, F. M., Arutyunov, K., 2006b. Phys. Rev. B 74, 052502.
- Shapira, Y., Deutsch, G., 1982. Thin Solid Films 87, 29.
- Sherman, D., Gorshunov, B., Poran, S., Trivedi, N., Farber, E., Dressel, M., Frydman, A., 2014. Phys. Rev. B 89, 35149.
- Silhanek, A. V., Raedts, S., Moshchalkov, V. V., 2004. Phys. Rev. B 70, 144504.
- Skocpol, W. J., Tinkham, M., 1975. Rep. on Prog. in Phys. 38, 1049.

- Skvortsov, M. A., Feigel'man, M., 2005. Phys. Rev. Lett. 95, 057002.
- Stewart, M. D., Yin, A., Xu, J. M., Valles, J. M., 2007. Science 315, 1273.
- Suslov, I., 2013. JETP 117, 1042.
- Suslov, I. M., 2015. arXiv:1501.05148.
- Tashiro, H., Graybeal, J., Tanner, D., Nicol, E., Carbotte, J., Carr, G., 2008. Phys. Rev. B 78, 014509.
- Tezuka, M., Garcia-Garcia, A. M., 2010. Phys. Rev. A 82, 43613.
- Thompson, C. J., Blatt, J. M., 1963. Phys. Lett. 5, 6.
- Tien, C., Pirozerskii, A. L., Charnaya, E. V., Xing, D. Y., Ciou, Y. S., Lee, M. K., Kumzerov, Y. A., 2011. J. Appl. Phys. 109, 053905.
- Tien, C., Wur, C. S., Lin, K. J., Charnaya, E. V., Kumzerov, Y. A., 2000. Phys. Rev. B 61, 14833.
- Tinkham, M., 1996. Introduction of Superconductivity. 2nd edition, McGraw Hill, Singapore.
- Tretyakov, V. V., Romanov, S. G., Fokin, A. V., Alperovich, V. I., 1998. Mikrochim. Acta Suppl. 15, 211.
- Uchihashi, T., Mishra, P., Aono, M., Nakayama, T., 2011. Phys. Rev. Lett. 107, 207001.
- Wang, X. L., Horvat, J., Liu, H. K., Dou, S. X., 1997. Physica C 282, 2125.
- Watson, J. H. P., 1970. Phys. Rev. 2, 1282.
- Yamada, M., Hirahara, T., Hasegawa, S., 2013. Phys. Rev. Lett. 110, 237001.
- Yang, G., Abell, J. S., Gough, C. E., 1997. Physica C 282, 2007.
- Yurchenko, V. V., Shantsev, D. V., Johansen, T. H., Nevala, M. R., Maasilta, I. J., Senapati, K., Budhani, R. C., 2007. Phys. Rev. B 76, 092504.
- Zhang, Y.-F., Jia, J.-F., Han, T.-Z., Tang, Z., Shen, Q.-T., Guo, Y., Qiu, Z. Q., Xue, Q.-K., 2005. Phys. Rev. Lett. 95, 096802.
- Zhou, Y.-H., Yang, X., 2006. Phys. Rev. B 74, 054507.